$Ca_V2.1$ α_1 Subunit Expression Regulates Presynaptic $Ca_V2.1$ Abundance and Synaptic Strength at a Central Synapse

Matthias Lübbert[3], **R. Oliver Goral**[1], **Christian Keine**[1], **Connon Thomas**[4], **Debbie Guerrero-Given**[4], **Travis Putzke**[3], **Rachel Satterfield**[3], **Naomi Kamasawa**[4], and **Samuel M. Young Jr.**[1,2,5,*]

[1]Department of Anatomy and Cell Biology, Iowa Neuroscience Institute, University of Iowa, Iowa City, IA 52242, USA

[2]Department of Otolaryngology, Iowa Neuroscience Institute, Aging Mind Brain Initiative, University of Iowa, Iowa City, IA 52242, USA

[3]Research Group Molecular Mechanisms of Synaptic Function, Max Planck Florida Institute for Neuroscience, Jupiter, FL 33458, USA

[4]Max Planck Florida Electron Microscopy Core, Max Planck Florida Institute for Neuroscience, Jupiter, FL 33458, USA

[5]Lead Contact

SUMMARY

The abundance of presynaptic Ca_V2 voltage-gated Ca^{2+} channels (Ca_V2) at mammalian active zones (AZs) regulates the efficacy of synaptic transmission. It is proposed that presynaptic Ca_V2 levels are saturated in AZs due to a finite number of slots that set Ca_V2 subtype abundance and that $Ca_V2.1$ cannot compete for $Ca_V2.2$ slots. However, at most AZs, $Ca_V2.1$ levels are highest and $Ca_V2.2$ levels are developmentally reduced. To investigate $Ca_V2.1$ saturation states and preference in AZs, we overexpressed the $Ca_V2.1$ and $Ca_V2.2$ α_1 subunits at the calyx of Held at immature and mature developmental stages. We found that AZs prefer $Ca_V2.1$ to $Ca_V2.2$. Remarkably, $Ca_V2.1$ α_1 subunit overexpression drove increased $Ca_V2.1$ currents and channel numbers and increased synaptic strength at both developmental stages examined. Therefore, we propose that $Ca_V2.1$ levels in the AZ are not saturated and that synaptic strength can be modulated by increasing $Ca_V2.1$ levels to regulate neuronal circuit output.

Graphical Abstract

In Brief

Lübbert et al. uncover that presynaptic active zones are not fully occupied by $Ca_V2.1$ during different states of neuronal circuit maturity. They propose that $Ca_V2.1$ levels in the presynaptic active zone can be increased to regulate neuronal circuit output.

INTRODUCTION

At central synapses, the Ca_V2 channel family, $Ca_V2.1$ (P/Q type), $Ca_V2.2$ (N type), and $Ca_V2.3$ (R type), mediate Ca^{2+} signals that trigger neurotransmitter release (Simms and Zamponi, 2014). Among the Ca_V2 family, $Ca_V2.1$ is dominant and most effective in triggering action potential (AP)-evoked release at the majority of central synapses (Eggermann et al., 2011; Iwasaki and Takahashi, 2001; Takahashi and Momiyama, 1993; Wheeler et al., 1994; Wu et al., 1998; Wu et al., 1999). A critical determinant of synaptic vesicle (SV) release probability (P_r) and release kinetics in response to APs is Ca_V2 subtype number (Ariel et al., 2013; Holderith et al., 2012; Sheng et al., 2012), which impacts synaptic strength (Schneggenburger and Rosenmund, 2015). In addition, Ca_V2 subtypes differentially control Ca^{2+} influx, which impacts synaptic transmission, plasticity, and strength (Catterall, 2011). Finally, presynaptic Ca_V2 subtype levels vary between synapses and can change with development and disease (Eggermann et al., 2011; Iwasaki and Takahashi, 2001; Momiyama, 2003; Scholz and Miller, 1995). Therefore, elucidating mechanisms regulating presynaptic Ca_V2 subtype levels is fundamental to understanding information encoding in the nervous system.

Since synaptic Ca_V2 levels at the AZ are distinct from the soma (Doughty et al., 1998; Miki et al., 2013), it is proposed that slots regulate Ca_V2 levels within the presynaptic AZ independent of the soma (Cao et al., 2004; Cao and Tsien, 2010). Although the molecular identity of slots is unknown, it is hypothesized that they differentially interact with the Ca_V2 α_1 subunit to set relative Ca_V2 levels and that slot preference can vary depending on synapse

type. It is thought some slots are $Ca_V2.2$ specific and that others prefer $Ca_V2.1$ but can accept $Ca_V2.2$, but that none are $Ca_V2.1$ exclusive and that these slots are always saturated (Cao et al., 2004; Cao and Tsien, 2010).

During neuronal circuit maturation, many presynaptic terminals either decrease the relative levels of $Ca_V2.2$ and $Ca_V2.3$ or shift to $Ca_V2.1$ exclusivity (Bucurenciu et al., 2010; Hefft and Jonas, 2005; Iwasaki et al., 2000; Iwasaki and Takahashi, 1998; Scholz and Miller, 1995). In addition, presynaptic Ca^{2+} currents are severely reduced with $Ca_V2.1$ α_1 subunit deletion and only slightly compensated for by increased $Ca_V2.2$ currents; while there is no compensation by $Ca_V2.3$ currents (Inchauspe et al., 2004; Lübbert et al., 2017). This suggests that at $Ca_V2.1$-dominated presynaptic terminals *in vivo*, $Ca_V2.1$-exclusive slots exist, and $Ca_V2.1$ are preferred over $Ca_V2.2$. More importantly, if slots existed in a $Ca_V2.1$-saturated state, this would constrain how $Ca_V2.1$-exclusive presynaptic terminals could increase Ca^{2+} entry to modulate synaptic strength and SV release kinetics and implies that increases in Ca^{2+} entry could only be achieved through $Ca_V2.1$ channel modulation, and not by increasing $Ca_V2.1$ levels in the presynaptic AZ.

To investigate the role of the Ca_V2 α_1 subunit in AZ preference and $Ca_V2.1$ saturation states at a $Ca_V2.1$ dominate presynaptic terminal, we used the calyx of Held, a giant axosomatic presynaptic terminal in the auditory brainstem which is similar to GABAergic cerebellar, thalamic, and hippocampal synapse and transitions from a mixed Ca_V2 subtype to $Ca_V2.1$ exclusivity during neuronal circuit maturation (Borst and Soria van Hoeve, 2012; Hefft and Jonas, 2005; Iwasaki et al., 2000). We used helper-dependent adenovirus (HdAd) viral vectors (Lübbert et al., 2017; Montesinos et al., 2016) and developed a surgery technique to overexpress $Ca_V2.1$ and $Ca_V2.2$ α_1 subunits before (mixed subtype) and after neuronal circuit maturation ($Ca_V2.1$ exclusive) to analyze their impact on $Ca_V2.1$ and $Ca_V2.2$ currents, channel numbers, and AP-evoked release. Here we show that $Ca_V2.1$ α_1 subunit overexpression leads to larger presynaptic Ca^{2+} currents due to increases in $Ca_V2.1$ currents and $Ca_V2.1$ channel number, which results in increased P_r at both developmental stages. In addition, we found that $Ca_V2.1$ channels, and not $Ca_V2.2$ channels, were preferred at both developmental stages. Therefore, we propose a modified "slot" model in which AZs are not fully occupied by $Ca_V2.1$ during different states of neuronal circuit maturity and that $Ca_V2.1$ can compete with other Ca_V2 subtypes. This implies that $Ca_V2.1$ levels in the AZ can be increased to regulate neuronal circuit output.

RESULTS

$Ca_V2.1$ α_1 Subunit Overexpression Increases $Ca_V2.1$ Currents with a Corresponding Loss of $Ca_V2.2$ in the Immature Calyx

To test if slots in synapses within a native neuronal circuit prefer $Ca_V2.1$ or $Ca_V2.2$ and whether Ca_V2 slots exist in a saturated state, we overexpressed the mouse $Ca_V2.1$ and $Ca_V2.2$ α_1 subunits at the P7 calyx of Held, a developmental time point at which the mouse calyx expresses a mixture of $Ca_V2.1$, $Ca_V2.2$, and $Ca_V2.3$ (~60% $Ca_V2.1$), similar to many other CNS synapses (Iwasaki et al., 2000; Iwasaki and Takahashi, 1998). We injected either $HdAdCa_V2.1$ α_1 or $HdAd$ $Ca_V2.2$ α_1 by utilizing the high-level overexpression cassette pUNISHER (Montesinos et al., 2011) to drive Ca_V2 α_1 expression, independent of an EGFP

or myristoylated EGFP (mEGFP) reporter, into the cochlear nucleus (CN) of P1 mice (Figures 1A-1C; Table S1). Viral particle to infectious unit ratios (VP:IU) of HdAd $Ca_V2.1$ α_1 or HdAd $Ca_V2.2$ α_1 were similar, therefore ensuring that $Ca_V2.1$ α_1 and $Ca_V2.2$ α_1 expression *in vivo* is equivalent. Using whole-cell voltage-clamp recordings at transduced or nontransduced P7 calyces, we measured the sensitivity of pharmacologically isolated Ca^{2+} currents (I_{Ca}) to the Ca_V2 subtype-specific blockers, ω-agatoxin IVA (Aga) ($Ca_V2.1$-selective) and ω-conotoxin GVIA (Cono) ($Ca_V2.2$-selective). All remaining Ca^{2+} currents ($Ca_V2.3$-mediated) were subsequently blocked with Cd^{2+} (nonspecific Ca_V2 channel blocker).

Measurements of the maximum steady-state I_{Ca} amplitudes in the absence of Ca_V2 blockers revealed a significant increase in the total I_{Ca} in the $Ca_V2.1$ α_1 overexpression (OE) calyces compared to control ($1{,}916 \pm 211$ pA versus 868 ± 51 pA, n = 4, n = 5, p = 0.0328, Mood's median test and *post hoc* Bonferroni test). However, this increase was absent in the $Ca_V2.2$ OE calyces (758 ± 132 pA, n = 6, p > 0.99, Mood's median test and *post hoc* Bonferroni test). Analysis of the Ca_V2 subtype contributions revealed the I_{Ca} increase in the $Ca_V2.1$ α_1 OE calyces was due to an ~3-fold increase in the Aga-sensitive current ($1{,}712 \pm 272$ pA versus 567 ± 66 pA, n = 4, n = 5, p = 0.0328, Mood's median test and *post hoc* Bonferroni test). In addition, we found a 65% decrease in the Cono-sensitive current (59 ± 26 pA versus 172 ± 26 pA, n = 4, n = 5, p = 0.0054, Mood's Median test and *post hoc* Bonferroni test) compared to control. Normalization of the Ca^{2+} currents revealed the contribution of $Ca_V2.1$ to I_{Ca} was strongly increased ($91\% \pm 3.2\%$ versus $65.2\% \pm 5.3\%$,) while the contribution of $Ca_V2.2$ ($3\% \pm 1.5\%$ versus $20.2\% \pm 3.1\%$) and $Ca_V2.3$ ($4.7\% \pm 2.3\%$ versus $14\% \pm 2.5\%$) were decreased (Figure 1I). In contrast, there were no changes in the toxin-sensitive fractions when overexpressing $Ca_V2.2$ α_1.

Since $Ca_V2.2$ activates at more positive voltages than $Ca_V2.1$ at the calyx (Inchauspe et al., 2004), it was possible that we underestimated the ability of $Ca_V2.2$ to compete for $Ca_V2.1$ slots. To further characterize how $Ca_V2.1$ and $Ca_V2.2$ α_1 OE influence I_{Ca}, we carried out current-voltage (IV) recordings (Figures 1J–1O). We switched to 1 mM external Ca^{2+} to minimize the potential influence of voltage clamp errors. Results of the IV relationships revealed that $Ca_V2.1$ α_1 OE increased I_{Ca} compared to control while $Ca_V2.2$ α_1 OE did not. The slow component of the cell capacitance (C_{slow}) in whole-cell configuration can be used as an estimate for the size of the presynaptic terminal. Since C_{slow} values were unchanged (Table S1), this indicates that I_{Ca} increases were not due to changes in calyx size. Fits of the presynaptic I_{Ca} revealed that $Ca_V2.2$ α_1 OE did not change the voltage dependence of activation. In summary, these results demonstrate that $Ca_V2.1$ α_1 OE leads to an increase in $Ca_V2.1$ currents which is paralleled by a reduction in $Ca_V2.2$ currents with no change in calyx size. Therefore, we conclude that presynaptic $Ca_V2.1$ current levels at the calyx of Held are not saturated and prefer $Ca_V2.1$ instead of $Ca_V2.2$.

The Increased Presynaptic $Ca_V2.1$ Currents Correspond to Increased $Ca_V2.1$ Numbers

To determine if the increased presynaptic $Ca_V2.1$ currents correlated to changes in $Ca_V2.1$ channel numbers, we carried out SDS-digested freeze fracture replica immunogold labeling (SDS-FFRL) at calyces transduced with either HdAd $Ca_V2.1$ α_1 OE mEGFP or

untransduced calyces (Figure 2; Table S2). Since Ca_V2 channels predominantly exist as clusters in the AZ (Baur et al., 2015; Budisantoso et al., 2012; Holderith et al., 2012; Indriati et al., 2013; Miki et al., 2017; Nakamura et al., 2015), we wanted to determine whether $Ca_V2.1$ numbers were increased specifically within clusters or randomly throughout the calyx. To do so, we used 30 nm radius circles extending from the center of each gold particle which accounts for Ca_V2 localization uncertainty (Althof et al., 2015) to measure the cluster area, number of gold particles per cluster, and gold particle density in clusters. We found that $Ca_V2.1$ α_1 OE resulted in a distribution shift to larger cluster areas which was evidenced by a mean increase in the cluster area (0.0122 ± 0.0004 μm^2 versus 0.0091 ± 0.0003 μm^2, p = 0.0006, Mann-Whitney U test), the number of gold particles per cluster (7.3 ± 0.3 versus 4.8 ± 0.2, $p < 0.0001$, Mann-Whitney U test), and the gold particle density per μm^2 cluster area (563.3 ± 4.2 versus 506.3 ± 4.6, $p < 0.0001$, Mann-Whitney U test) (Figures 2B–2D). In addition, we found a decrease of inter-particle distance per cluster (Table S2) and that there was a decrease in the number of single gold particles not found in a cluster compared to control (4.8% versus 10.9%, $p < 0.0001$, Fisher's exact test) (Figure 2E), indicating the increased number of $Ca_V2.1$ channels lead to a higher probability of $Ca_V2.1$ channels being in clusters. Finally, these changes were not due to mEGFP expression, as previous reports have demonstrated that mEGFP expression alone does not lead to increases in Cav2.1 numbers (Dong et al., 2018).

Individual presynaptic AZs contain multiple Ca_V2 clusters in a nonrandom organization (Holderith et al., 2012; Indriati et al., 2013; Nakamura et al., 2015). Therefore, we wanted to determine if $Ca_V2.1$ α_1 OE increased the number of $Ca_V2.1$ channels and clusters within the AZ. At the calyx, a 100 nm radius extending from the center of the gold particle is equivalent to the average putative AZ area (Dong et al., 2018). Thus, we used a 100 nm radius from individual gold particles to measure the putative AZ area, the number of gold particles, particle density, and the 30 nm cluster distribution within the putative AZ (Figures 2F and 2G; Table S2). We found that $Ca_V2.1$ α_1 OE increased the putative AZ area (0.153 ± 0.011 μm^2 versus 0.105 ± 0.008 μm^2, p = 0.0015, Mann-Whitney U test) and a corresponding increase gold particle density within the putative AZ (110.8 ± 2.6 versus 86.6 ± 2.2, $p < 0.0001$ Mann-Whitney U test). Subsequently, we counted the number of 30 nm clusters (>1 particle within 30 nm area) within the putative AZ. Our analysis revealed a shift towards putative AZs with increased cluster numbers (2.44 ± 0.17 versus 1.59 ± 0.14, $p < 0.0001$, Mann-Whitney U test; Figure 2G). Taken together, our results demonstrate that the increase in presynaptic $Ca_V2.1$ currents upon $Ca_V2.1$ α_1 OE correlates with increased $Ca_V2.1$ numbers, density per cluster, and cluster numbers.

Increased $Ca_V2.1$ Channels Numbers Do Not Change AZ Ultrastructure

Our SDS-FFRL data demonstrated that the putative AZ at the calyx increases in size with $Ca_V2.1$ α_1 OE. However, the putative AZ area is based on $Ca_V2.1$ numbers and therefore an indirect measurement of AZ size. To directly measure the AZ length, we carried out ultrathin section TEM on the $Ca_V2.1$ α_1 OE calyces and control (Figure 3; Table S2). The presynaptic AZ was defined as the membrane opposing the postsynaptic density (PSD) (Clarke et al., 2012). We found no increase in AZ length compared to control (Figures 3B and 3C). Since $Ca_V2.1$ clusters are suggested to correlate to SV docking sites (Miki et al., 2017), we

measured the number of docked SV, defined as those within 5 nm of the plasma membrane (Taschenberger et al., 2002). Analysis of SV distribution revealed no change in docked SV number or SV distribution (Figures 3D and 3E). Our data demonstrate that AZ length and SV docking do not change with an increase in $Ca_V2.1$ channel numbers at the AZ. Therefore, we conclude that the AZ area does not increase to accommodate more $Ca_V2.1$ channels.

Increase in Presynaptic Cav2.1 Numbers Do Not Impact Quantal Amplitude

Although our ultrastructural data indicated there were no changes in AZ ultrastructure, it was possible that there were changes in SV volume that would not be apparent in the ultrathin section EM. Therefore, we recorded spontaneous AMPA-mediated miniature excitatory postsynaptic currents (mEPSC) in medial nucleus of the trapezoid body (MNTB) principal cells innervated by transduced or non-transduced calyces (Figures 3F–3H). We found no change in the mEPSC amplitudes between the $Ca_V2.1$ α_1 OE and control calyces (37.2 ± 1.6 pA versus 35.7 ± 1.9 pA, p = 0.56, two-tailed t test, n = 15), while there was an ~2-fold increase in the mEPSC frequency (0.56 ± 0.1 Hz versus 0.92 ± 0.1 Hz, p = 0.04, two-tailed t test, n = 15). Since quantal amplitude was not increased, we conclude that $Ca_V2.1$ α_1 OE does not lead to an increase in SV volume.

Increased Presynaptic $Ca_V2.1$ Numbers Result in Increased Pr

The strength of neurotransmitter release in response to APs is positively correlated to Ca_V2 numbers within the AZ (Holderith et al., 2012; Sheng et al., 2012), and AP-evoked release is highly dependent on the positioning of SVs relative to VGCCs (Neher, 2010). Since our EM data suggested that $Ca_V2.1$ numbers were increased within the AZ, this would significantly increase synaptic strength. However, if $Ca_V2.1$ channels were inserted outside the AZ, this would lead to no change in synaptic strength. To determine if the observed $Ca_V2.1$ channel increase impacts AP-evoked release, we carried out afferent fiber stimulation of the calyx axons and recorded the AMPAR-mediated EPSCs from the MNTB principal cells innervated by transduced or non-transduced calyces (Figure 4; Table S3). We measured AP-evoked synaptic transmission using a stimulation frequency of 0.05 Hz (in 1.2 mM $[Ca^{2+}]_{ext}$, Figures 4A–4C). Our analysis revealed a dramatic increase in AP-evoked EPSC of the $Ca_V2.1$ α_1 OE versus control (3.1 ± 0.37 nA versus 1.47 ± 0.21 nA, p = 0.0006, Mann-Whitney, n = 20), while normalized EPSC waveforms and analysis of rise time and half-width indicated no change in EPSC kinetics (Figure 4C).

Although the RRP has been correlated to the morphologically docked SVs (Schikorski and Stevens, 2001), recent data suggest otherwise (Sakamoto et al., 2018). Therefore, despite no change in docked SV number (Figure 3), the increased AP-evoked release could be due to either an increase in the readily releasable pool (RRP) size, an increase in the initial P_r, or both. To measure the RRP size, we carried out 50 Hz stimulation and used an SMN plot with correction for incomplete pool depletion (Neher, 2015) or fitting with a pool depletion model (NpRf model) (Thanawala and Regehr, 2016). Both analysis methods indicated that increased $Ca_V2.1$ numbers did not lead to an increase in RRP size. Calculation of initial P_r by dividing the first EPSC by the RRP size demonstrated that $Ca_V2.1$ α_1 OE calyces had a significant increase in initial P_r compared to control (SMN, 0.34 ± 0.04 versus 0.2 ± 0.03, p

= 0.033, Mann-Whitney U test; NpRf, 0.31 ± 0.05 versus 0.19 ± 0.03, $p = 0.045$, Mann-Whitney U test, $n = 20$, $n = 17$). The increase in P_r was further confirmed as normalization of the EPSC in the trains to the first EPSC demonstrated an increased rate of depression in the $Ca_V2.1$ α_1 OE calyces compared to control. These results demonstrate that the higher $Ca_V2.1$ channel numbers by $Ca_V2.1$ α_1 OE resulted in increased synaptic strength that is due to increases in P_r. Thus, we conclude that additional $Ca_V2.1$ channels resulting from $Ca_V2.1$ α_1 OE are located within the AZs and that $Ca_V2.1$ channel levels are not saturated in the AZ.

$Ca_V2.1$ α_1 Overexpression Increases $Ca_V2.1$ Current Levels in the Mature Calyx of Held

Around the onset of hearing in mice at ~P12, the calyx of Held becomes a $Ca_V2.1$-exclusive terminal (Doughty et al., 1998; Iwasaki and Takahashi, 1998), similar to many cerebellar, thalamic, and other auditory brainstem synapses (Iwasaki et al., 2000). By ~P14, the calyx has undergone AZ ultrastructure refinement (Taschenberger et al., 2002) and supports adult-like auditory processing (Sonntag et al., 2009, 2011). Furthermore, by P18 the calyx of Held/MNTB synaptic responses to sound is indistinguishable from that in adult animals (Sonntag et al., 2009).Therefore, it was imperative to determine if our findings were specific to an early developmental stage or also applied to synapses in a mature neuronal circuit. Therefore, we developed a stereotactic surgery to target the CN in P14 mice (Figures 5A and 5B; Table S4) and subsequently measured how $Ca_V2.1$ and $Ca_V2.2$ α_1 OE impacted $Ca_V2.1$ levels, organization, AZ ultrastructure, and synaptic transmission at the adult-like P20/P21 calyx.

To test if $Ca_V2.2$ could compete for $Ca_V2.1$ slots in a $Ca_V2.1$-exclusive synapse, we injected $Ca_V2.2$ α_1 OE virus into the P14 CN and then measured I_{Ca} sensitivity to Aga and Cono at either untransduced or transduced P20/P21 calyces (Figures 5C-5E). Similar to the results at P7, $Ca_V2.2$ α_1 OE did not increase the total I_{Ca}. Fractional current analysis revealed that $Ca_V2.2$ α_1 OE led to small $Ca_V2.2$ currents (Figure 5D) amounting to ~10% of the overall I_{Ca} amplitude not found in controls (125 ± 37 pA versus 3 ± 3 pA, $p = 0.016$, $n = 3$, t test). To determine if $Ca_V2.1$-mediated increases were dependent on the developmental stage, we injected $Ca_V2.1$ α_1 OE virus and recorded I_{Ca}. Our results demonstrated that $Ca_V2.1$ currents were increased compared to control (Figures 5F–5H) (Table S4), while normalization and fits revealed a change in I_{Ca} kinetics. In addition, we found no increase in C_{slow}, indicating that the increase in I_{Ca} is not due to a parallel increase in calyx size. Based on these results, we conclude that $Ca_V2.1$ preference and $Ca_V2.1$ increases are not restricted to an early developmental stage.

The Increased $Ca_V2.1$ Currents Correspond to Increased $Ca_V2.1$ Numbers in the Mature Calyx

Since the calyx undergoes morphological changes at hearing onset, it was important to know how $Ca_V2.1$ numbers and their organization were impacted upon $Ca_V2.1$ OE. Therefore, we applied an identical approach as performed at P7 to conduct SDS-FFRL at either transduced or untransduced calyces at P21 (Figure 6; Table S5). Using a 30 nm radius to measure $Ca_V2.1$ clustering, we measured the cluster area, number of gold particles per cluster, and cluster particle density. We found that $Ca_V2.1$ α_1 OE resulted in a shift in the distribution to

larger cluster areas (0.0118 ± 0.0006 μm^2 versus 0.0094 ± 0.0004 μm^2, p = 0.0315, Mann-Whitney U test) and a parallel increase in the number of gold particles per cluster (6.8 ± 0.4 versus 5.4 ± 0.3, p = 0.0139, Mann-Whitney U test). Analysis of the gold particle density per cluster and inter-particle distance in Ca$_V$2.1 α$_1$ OE versus control showed no difference, indicating that cluster areas grew to accommodate increased Ca$_V$2.1 channel numbers (Figure 6D; Table S5). Finally, we found no change in the cluster density on the P-face.

Subsequently, we measured putative AZ area and the number of gold particles, particle density, and cluster distribution within the putative AZ (Figures 6F and 6G). Analysis of the putative AZ area in the Ca$_V$2.1 α$_1$ OE condition revealed a shift in the distribution to putative AZs with larger size (0.116 ± 0.008 μm^2 versus 0.102 ± 0.011 μm^2, p = 0.0075 Mann-Whitney U test). We found an increase in gold particle density per putative AZ, indicating that putative AZs were larger and contained more gold particles (105.9 ± 3.3 versus 88.8 ± 3.2, p = 0.001 Mann-Whitney U test) (Table S5). Counts of the number of 30 nm clusters within the putative AZ revealed no change in cluster numbers within the putative AZs (Figure 6G). Furthermore, there was no change in relative frequency in the number of single particles within the putative AZ with Ca$_V$2.1 OE versus control. Taken together, our results revealed that increases in Ca$_V$2.1 current were correlated with increases in the Ca$_V$2.1 numbers and density per cluster, but not cluster numbers within the putative AZ. Therefore, we conclude that AZs are not saturated for Ca$_V$2.1 channels in the mature presynaptic terminal.

Ca$_V$2.1 α$_1$ OE Leads to Smaller AZs and a Reduction in SV Docking at the P21 Calyx

To determine if AZs increased in size to accommodate more Ca$_V$2.1 channels, we performed ultrathin section TEM at the P21 Ca$_V$2.1 α$_1$ OE calyces and control (Figure 7; Table S5). Analysis of the AZ length revealed that Ca$_V$2.1 α$_1$ OE calyces (Figure 7B) had slightly smaller AZs compared to control (329.9 ± 8.2 nm versus 376.7 ± 12.2 nm, p = 0.0339, Mann-Whitney U test). In addition, we found a reduced number of docked SVs (1.0 ± 0.09 versus 1.8 ± 0.12, p < 0.0001 Mann-Whitney U test) (Figures 7D and 7E). For this reason, we conclude that the AZ can accept more Ca$_V$2.1 channels without increasing in size and that Ca$_V$2.1 levels in the AZ are not saturated in the mature calyx.

Increased Ca$_V$2.1 Numbers Result in Increased P_r in the Mature calyx

The mature calyx of Held utilizes nanodomain release modality to support the initial stages of auditory processing in adult animals (Fedchyshyn and Wang, 2005). Since single Ca$_V$2.1 channels can trigger SV fusion in response to APs in nanodomain release modality (Stanley, 2016), it was important to determine how Ca$_V$2.1 channel increases in the AZ impact synaptic strength at the P20/21 calyx. First, to determine if there were changes in quantal amplitudes (Figure 7), we measured spontaneous release at the P20/21 calyces. Analysis revealed no change in mEPSC frequency or amplitudes (Figures 7F–7H; Table S5). Subsequently, we carried out afferent fiber stimulation in 1.2 mM [Ca^{2+}]$_{ext}$ to mimic *in vivo* P_r (Lorteije et al., 2009) and measured AP-evoked release (Figure 8; Table S6). In response to 0.05 Hz stimulation, we found an ~6-fold increase in the AP-evoked EPSC amplitude of Ca$_V$2.1 α$_1$ OE calyces compared to control (3.64 ± 0.6 nA versus 0.57 ± 0.1 nA, p < 0.0001, Mann-Whitney U test, n = 15, n = 10), while analysis of the EPSC waveforms indicated no

change in the release kinetics. To determine if the increase in AP-evoked release was due to an increase in RRP or initial P_r, we conducted fiber stimulation at 300 Hz, which is similar to sound-evoked firing rates (Sonntag et al., 2009). Analysis of the RRP size revealed a dramatic increase of the RRP in the $Ca_V2.1$ α_1 OE calyces for both the SMN and NpRf method (Figure 8I). Calculation of initial P_r by dividing the first EPSC by the RRP size demonstrated that $Ca_V2.1$ α_1 OE increased initial P_r compared to control (SMN, 0.19 ± 0.03 versus 0.08 ± 0.02, p = 0.0024, Mann-Whitney U test; NpRf, 0.18 ± 0.03 versus 0.07 ± 0.01 versus, p = 0.0067, two-tailed t test, n = 14, n = 10). The increase in P_r was further confirmed as we found reduced facilitation and an increased rate of depression in the $Ca_V2.1$ α_1 OE calyces versus control. These results demonstrate that the increase in $Ca_V2.1$ channels results in increased synaptic strength that is due to increases in both the P_r and the RRP in the mature calyx of Held. Therefore, we conclude that the increased $Ca_V2.1$ channel numbers are located within the AZs and that AZs are not saturated *in vivo*.

DISCUSSION

By overexpressing the $Ca_V2.1$ and $Ca_V2.2$ α_1 subunits in a native neuronal circuit at two distinct developmental stages, we determined $Ca_V2.1$ and $Ca_V2.2$ preference and saturation states at the presynaptic AZ and their impact on synaptic transmission and plasticity. Based on our data, we conclude that *in vivo* presynaptic AZs with mixed Ca_V2 composition which are $Ca_V2.1$ dominate, or $Ca_V2.1$ exclusive are not saturated for $Ca_V2.1$ and prefer $Ca_V2.1$. Therefore, we propose that synaptic plasticity and strength can be modulated by increasing $Ca_V2.1$ levels in both mixed Ca_V2 and $Ca_V2.1$-exclusive synapses to increase efficacy and to diversify information encoding by neuronal circuits.

In general, our results contrast with studies based on primary cultured CA3/CA1 hippocampal neurons at mixed Ca_V2 subtype, $Ca_V2.1$ dominate synapses (Cao et al., 2004; Cao and Tsien, 2010; Hoppa et al., 2012; Schneider et al., 2015). The ability of $Ca_V2.1$ α_1 OE to increase $Ca_V2.1$ levels may be due to conditions specific to the network activity of the native neuronal circuits which is not replicated in *in vitro* cultured neuronal circuits. Since the $Ca_V\beta$ and $\alpha_2\delta$ auxiliary subunits of the Ca_V2 channel complex and the synprint region are critical for trafficking Ca_V2 channels to the presynaptic terminal and control Ca_V2 levels in the plasma membrane (Catterall, 2011), it is possible that these trafficking pathways to the presynaptic terminal are saturated for $Ca_V2.1$ in cultured hippocampal neurons, but not in a native setting. Finally, we only analyzed the impact of chronic $Ca_V2.1$ overexpression 6–7 days post-expression, while prior studies measured $Ca_V2.1$ levels at the presynaptic terminal after 2 weeks post-expression (Hoppa et al., 2012; Schneider et al., 2015). Thus, it is possible that chronic overexpression of $Ca_V2.1$ on the time course of weeks may result in a homeostatic reduction in $Ca_V2.1$ levels at the calyx.

In previous studies, $Ca_V2.2$ α_1 OE led to a complete loss of $Ca_V2.1$-mediated AP-evoked release (Cao and Tsien, 2010; Schneider et al., 2015). However, it is important to note that our experimental paradigms were different. We used HdAd vectors (Montesinos et al., 2016) in combination with high-level transgene expression, pUNISHER (Chen et al., 2013; Montesinos et al., 2011; Young and Neher, 2009), to overexpress the mouse $Ca_V2.1$ and $Ca_V2.2$ α_1 subunit in a synapse within its native neuronal circuit at two well-defined

developmental time points. In contrast, prior studies expressed human $Ca_V2.1$ and human or rabbit $Ca_V2.2$ α_1 subunit cDNA in a mixed population of hippocampal synapses at an *in vitro* neuronal circuit. Therefore, the differences in our results are likely due to multiple reasons: differences between cDNAs used (mouse versus human, rabbit), synapse types, synapse developmental stages, neuron environment *in vivo* versus *in vitro*, and use of SDS-FFRL immuno-EM versus fluorescence microscopy to detect $Ca_V2.1$ levels in the presynaptic terminal.

Our findings demonstrate that $Ca_V2.1$ current increases were correlated with increased $Ca_V2.1$ channel numbers with no changes in AZ zone size and provide evidence for the existence of unoccupied slots at the AZ. Our SDS-FFRL immune-EM measurements detected on average a 2- to 3-fold channel increase per 30 nm cluster at both the P7 and the P21 plasma membrane, which represents a 40% and 20% increase, respectively. Furthermore, at both developmental time points we found an increase in gold particle density per cluster area. However, although we found a decrease in the inter-particle distance in P7 $Ca_V2.1$ OE calyces, we found no change at P21. Since $Ca_V2.1$ channels represent only ~60%–70% of I_{Ca} at the P7 calyx, while the P20/21 calyx is $Ca_V2.1$ exclusive, the 40% increase at P7 compared to the 20% increase at P21 is likely due to the replacement of $Ca_V2.2$ with $Ca_V2.1$ in addition to filling the unoccupied slots and may explain the ability to more tightly pack $Ca_V2.1$ channels at P7 compared to P21. More importantly, since we found an increase in gold particle density but not a decrease in the inter-particle distance in $Ca_V2.1$ clusters at the P21 calyx, this suggests there is a limit on the packing of $Ca_V2.1$ channels. Regardless, in both cases these levels of increase are likely not detectable in studies using fluorescent measurements to qualitatively count $Ca_V2.1$ numbers due to technical limitations (Hoppa et al., 2012; Schneider et al., 2015). However, overexpression of a $Ca_V2.1$ α_1 EGFP tagged subunit did lead to an ~20% increase in EGFP signal in presynaptic boutons (Hoppa et al., 2012). Since AP-evoked release is highly dependent on the location of Ca_V2 channels within the AZ (Schneggenburger and Rosenmund, 2015), it is an indirect readout of Ca_V2 channel localization. Thus, our observation that AP-evoked release was dramatically increased indicates that $Ca_V2.1$ channels were localized within the AZ.

Since defining the AZ with SDS-FFRL immuno-EM is difficult (Hagiwara et al., 2005; Holderith et al., 2012; Indriati et al., 2013; Miki et al., 2017; Nakamura et al., 2015), it was possible that AZ size increased to accommodate more channels. Although we were unable to accurately measure the AZ area with SDS-FFRL immuno-EM technique due to the lack of presynaptic morphological signatures, we relied on using a 100 nm radius to measure the putative AZ area, the rationale being that the putative AZ sizes measured under control conditions are similar to previous AZ area measurements using ultrathin section TEM (Dong et al., 2018; Sätzler et al., 2002; Taschenberger et al., 2002). However, our putative AZ measurements are inherently biased, since they depend on $Ca_V2.1$ labeling. For example, we likely underestimated the putative AZ size at the P7 calyx in our control calyces by 30% –40%, since $Ca_V2.1$ channels represent only ~60%–70% of I_{Ca}. Heavy metal staining with ultrathin TEM using the PSD density as a measure of presynaptic AZ length is independent of Ca_V2 labeling and therefore a more accurate measure of AZ length, since AZ and PSD

scale in a 1:1 manner (Clarke et al., 2012). However, we cannot rule out that the presynaptic AZ increased independent of the postsynaptic side.

The molecular identity of slots is unknown. Currently, there is no correlation between the levels of key AZ proteins implicated to control either $Ca_V2.1$ and $Ca_V2.2$ levels at different synapses (Althof et al., 2015; Holderith et al., 2012; Indriati et al., 2013; Lenkey et al., 2015; Miki et al., 2017; Nakamura et al., 2015). Although RIMs (Han et al., 2011; Kaeser et al., 2011; Müller et al., 2012) and CAST/ELKS (Dong et al., 2018; Kittel et al., 2006) control Ca_V2 levels, currently bassoon is the only AZ protein proposed to specifically control $Ca_V2.1$ channel levels compared to $Ca_V2.2$ channels (Davydova et al., 2014). However, mutant $Ca_V2.1$ channels lacking the bassoon binding interaction domain can rescue $Ca_V2.1$ channel levels similarly to wild-type levels (Lübbert et al., 2017). Additionally, knockdown of bassoon or combined knockout of bassoon and piccolo has no effect on basal AP-evoked release at the $Ca_V2.1$ exclusive calyx (Parthier et al., 2018), and $Ca_V2.1$ and $Ca_V2.2$ mEOS-tagged protein levels appear to be equivalent at bassoon-positive punctae (Schneider et al., 2015).

Alternatively, it is possible that slots do not exist. Evidence in support of this hypothesis comes from work in *Drosophila*, where it was demonstrated that Ca_V2 channels arrive first at the presynaptic plasma membrane and are then followed by AZ proteins (Fouquet et al., 2009). In addition, $Ca_V2.2$ and $Ca_V2.1$ have been found to be interspersed and not mutual exclusive within the presynaptic AZ (Lenkey et al., 2015). However, whether this is universal to all presynaptic AZs is not known, as specific antibody staining for $Ca_V2.2$ is difficult because the conditions for specific staining in different presynaptic AZs need to be developed. Regardless, in the scenario in which slots do not exist, multiple processes that control Ca_V2 trafficking, insertion, retention, and stability to the plasma membrane may all contribute to give the appearance of a slot in the AZ. Thus, differences between the different Ca_V2 α_1 subunits and their interactions with $Ca_V\beta$, synprint sites, AZ proteins (Catterall, 2011; Müller et al., 2010; Simms and Zamponi, 2014), and ubiquitination pathways (Felix and Weiss, 2017) will be critical for Ca_V2 subtype levels in the AZ. In addition, alternative splicing of Ca_V2 α_1 subunits which impacts these pathways will diversify Ca_V2 α_1 presynaptic specificity (Lipscombe et al., 2013). Finally, since many AZ protein isoforms are expressed in different synapses (Nusser, 2018), it is likely that Ca_V2 preference in the AZ varies between synapses and with development. In support of this scenario, we found variable competition in $Ca_V2.2$ α_1 OE for $Ca_V2.1$ channels at the P7 calyx, suggesting that AZs at P7 calyces are not homogenous for Ca_V2 preference, and we found that $Ca_V2.2$ α_1 OE results in appearance of a small $Ca_V2.2$ current that corresponded to ~10% of the overall I_{Ca} in the P21 calyx. In addition, $Ca_V2.2$ channels cannot entirely compensate for the loss of $Ca_V2.1$ channels at the calyx (Inchauspe et al., 2004) or in mature CA1 hippocampal neurons (Mallmann et al., 2013). Finally, although $\alpha_2\delta$ proteins are critical for Ca_V2 channel trafficking, a previous report indicates that $\alpha_2\delta$ proteins do not differentially regulate individual Ca_V2 subtype levels (Hoppa et al., 2012). Although $\alpha_2\delta$ overexpression led to increased Ca_V2 channel numbers (Hoppa et al., 2012; Schneider et al., 2015), this was paralleled by increases in AZ size (Schneider et al., 2015).

The prehearing calyx utilizes microdomain release (Bollmann et al., 2000; Schneggenburger and Neher, 2000), while the P21 calyx utilizes nanodomain release (Fedchyshyn and Wang, 2005). The increased synaptic strength at $Ca_V2.1$ α_1 OE was caused by higher P_r at P7, while at P20/21 both P_r and RRP were increased with no change in quantal amplitude. These findings suggest that $Ca_V2.1$ level increases differentially impact synaptic strength in microdomain and nanodomain release synapses. What could be the reasons? Recent work has suggested that $Ca_V2.1$ cluster numbers in the presynaptic plasma membrane correlate to the functional RRP size in $Ca_V2.1$ nanodomain synapses (Miki et al., 2017). However, at P21 we found no increases in the number of $Ca_V2.1$ clusters in the putative AZs. Although SV docking is considered the morphological correlate of the functional RRP (Rollenhagen et al., 2007), our morphological data from P20/21 calyces demonstrate a reduction in SV docking that is not in agreement with the functional RRP size. In addition, although we found larger $Ca_V2.1$ clusters in P7 calyces, we did not find increases in SV docking. This discrepancy may be due to our fixation methods using PFA, which may not accurately represent SV docking states (Siksou et al., 2007) and may result in preferential depletion of docked SVs in the $Ca_V2.1$ OE calyces during PFA fixation (Smith and Reese, 1980). Regardless, prior studies indicate that SV docking does not correlate with the functional RRP size (Neher, 2015; Sakamoto et al., 2018; Thanawala and Regehr, 2013). Although changes in post-priming can increase SV fusogenicity which increases mEPSC frequency and the functional RRP size (Basu et al., 2007), we found no change in mEPSC frequencies in P20/21 $Ca_V2.1$ OE terminals, indicating post-priming changes that increase SV fusogenicity are not responsible for the increase RRP size.

Although individual AZs have multiple release sites (Maschi and Klyachko, 2017), recent modeling studies have indicated that a perimeter release model accurately reproduces calyx release characteristics (Chen et al., 2015; Nakamura et al., 2015). In this model, increases of $Ca_V2.1$ number will increase P_r at individual release sites, which will lead to increases in AP evoked release. However, one Ca_V2 channel can theoretically trigger SV release at nanodomain synapses due to tight coupling (Stanley, 2016). Therefore, it is possible that increases in the perimeter due to more $Ca_V2.1$ channels lead to the RRP increase only in the mature calyx. In this scenario, since increases in $Ca_V2.1$ will increase the number of open $Ca_V2.1$ channels in response to APs, the tight coupling state will increase the probability that SVs located around the perimeter will be released in response to repetitive AP stimulation.

In summary, our findings counter prevailing views that $Ca_V2.1$ channel levels are saturated at presynaptic active zones. Since modulation of synaptic strength is a fundamental process that regulates synaptic transmission and plasticity and Ca_V2 channels are key targets of regulation (Davis and Müller, 2015), our findings provide important insights into how $Ca_V2.1$ channels are modulated to regulate synaptic transmission and plasticity at different synaptic release modalities in native neuronal circuits. Future studies will resolve the molecular mechanisms and their signaling pathways and physiological conditions by which Ca_V2 levels are regulated at the presynaptic active zone in different synapses.

STAR★METHODS

CONTACT FOR REAGENT AND RESOURCE SHARING

Further information and requests for resources and reagents should be directed to and will be fulfilled by the Lead Contact, Samuel M. Young, Jr., at samuel-m-young@uiowa.edu.

DATA AND SOFTWARE AVAILABILITY

Custom written software used for series resistance compensation and offset correction used in this study is available as part of the Patcher's Power Tools (RRID:SCR_001950). Other custom software used in this study is available under https://doi.org/10.17632/4ycrjtpfc6.1.

EXPERIMENTAL MODEL AND SUBJECT DETAILS

Animals—For all experiments C57Bl6 mice (Jackson Laboratories; RRID:IMSR_JAX: 000664) of both sexes at age P7 or P20/P21 were used for analysis, while both sexes were used at age P1 or P14 for stereotaxic surgery. Animals were bred in-house at 12/12h light/dark cycle and had access to food and water *ad libitum*. All procedures were performed in accordance with the animal welfare laws of the Max Planck Florida Institute for Neuroscience and University of Iowa Institutional Animals Care and Use Committee and complied with accepted ethical best practice.

METHOD DETAILS

Helper-Dependent Adenoviral vectors—The $Ca_V2.1$ α_1 (*Mus musculus*, Accession No.: NP_031604.3) or $Ca_V2.2$ α_1 subunit cDNA (*Mus musculus*, Accession No.: NP_001035993.1) were each codon optimized for expression in mouse (GeneArt) and cloned individually into the EcoRI and NotI sites of the pUNISHER expression cassette (Montesinos et al., 2011; Young and Neher, 2009). Next, the expression cassettes were cloned into pdelta28E4 (kindly provided by Dr. Philip Ng) (Palmer and Ng, 2003) which also contained a separate neurospecific expression cassette to drive either EGFP or mEGFP (Lübbert et al., 2017). The final HdAd plasmid allows for expression of $Ca_V2.1$ or $Ca_V2.2$ independently of EGFP or mEGFP.

Production of HdAd was carried out as previously described (Montesinos et al., 2016; Palmer and Ng, 2011). Briefly, pHdAd was linearized by *Pmel* to expose the ends of the 5' and 3' inverted terminal repeats (ITRs) and then transfected into 116 producer cells (Profection® Mammalian Transfection System, Promega). For HdAd production, helper virus (HV) was added the following day. 48h post infection, after cytopathic effect (CPE), cells were subjected to three freeze/thaw cycles. Lysate was amplified in a total of five serial coinfections of HdAd and HV from $3\times$ 6 mm tissue culture dishes followed by a 15 cm dish and finally 30×15 cm dishes of 116 cells (confluence ~90%). HdAd was purified by CsCl ultracentrifugation and stored at $-80\,°C$ in storage buffer (in mM): 10 HEPES, 250 sucrose, 1 $MgCl_2$ at pH 7.4.

HdAd titering and quality control—HdAds were titered by qPCR as described previously (Puntel et al., 2006). The purified reference virus (RV); Ad5-CMV-EGFP (UNC, Gene Therapy Center, Chapel Hill, North Carolina) was titered by endpoint dilution and by

transducing units, as described previously (Bewig and Schmidt, 2000). Human Adenovirus 5 Adenovirus Reference Material (ARM) was purchased from ATCC (VR-1516) (Palmer and Ng, 2003). To titer the HdAd by qPCR, adenoviral gDNA from HdAd, RV and ARM was purified from 6 cm plates. Plates were seeded with 3.75×10^6 HEK293 cells in DMEM with 10% FBS and coinfected with HdAd plus RV on the following day at a multiplicity of 100 vp/cell. The cells were incubated for 1 hr at 37°C with 5% CO_2 and washed to remove unabsorbed virions. Cells were harvested 4 hr post-infection, then washed with 1 mL PBS and centrifuged for 5 min at 4°C. Pellets were resuspended in 100 mM Tris-HCl, pH 8, lysed by freeze/thaw cycles and treated with 20 U/mL Benzonase for 10 min. Subsequently, lysate was incubated in ProtK-SDS solution for 3 hr at 50°C. After protein precipitation with 1.65 M NaCl on ice, DNA was precipitated from supernatants with isopropanol and 3 M sodium acetate, pH 5.2. Samples were mixed well and incubated for 1 hr at −80°C then spun at 4°C for 30 min. Pellets were washed with cold ethanol, dried and resuspended in 10 mM Tris-Cl, pH 8.0. A plasmid standard containing three specific DNA sequences; Ad5 E1a (replication-competent Adenovirus (RCA) detection), Ad5 E2B Iva2 (viral DNA polymerase and terminal protein precursor, HV-exclusive), and Ad genomic stuffer sequence (Cosmid 346 and HPRT1 gene, in all HdAd-exclusive) was used. Three specific primer/probe sets were used for these 3 regions in the plasmid for the detection in qPCR:

1. **Ad5 E1a (RCA):** probe: NED-5'-AGCACCCCGGGCACGGTTG-3'-MGBNFQ; fwd: 5'-GGGTGAGGAGTTTGTGTTAGATTA TG-3'; rev: 5'-TCCTCCGGTGATAATGACAAGA-3'

2. **E2B Iva2 (HV):** probe: FAM-5'-TGTCTTTCAGTAGCAAGCT-3'-TAMRA, HV fwd primer: 5'-TGGGCGTGGTGCCTAAAA-3', rev: 5'-GCCTGCCCCTGGCAAT-3'

3. **Genomic stuffer DNA (HdAd):** probe: VIC-5'-AGCCTCTCTCATCTCACAGT -3'-MGBNFQ, fwd: 5'-CCCCGCTACCCCA ATCC-3', rev: 5'-TTAGCTTTTTTGGGTGATTTTTCC-3'.

Sample DNA was diluted $1:10^3$, $1:10^4$ or 10^5 in 10 mM Tris-Cl, pH 8.0. For HdAd and HV probes, a 6-point standard curve was constructed with the plasmid standard using 10^7- 10^2 molecules/well. For RCA detection, two 7-point curves were constructed with 10^7 - 10 molecules/well (one plasmid standard and one using ARM gDNA spiked with 10^7 copies of HdAd gDNA). Real-Time PCR parameters were 50°C for 2 min, 95°C for 10 min; 40 cycles of: 95°C for 15 sec, 60°C for 1 min. Outliers and results out of range of standard curve were discarded. Results within range of the standard curve were corrected for their dilution and determined as HdAd vector genomes/mL. All samples were negative for RCA.

To determine the IU copies/mL from purified coinfection samples, averaged results were divided by 3 μL and multiplied by 25 μL giving IU copies/coinfection. Next, this number was divided by the volume in μL of HdAd added to the coinfection giving IU copies/μL then multiplied by 1000 to obtain the Infectious HdAd genomes/mL.

Calculation to determine the titer of purified HdAd virus:

$$HdAd\ infectivity = RV\ infectivity * \frac{HdAd\ vector\ genomes\ /\ RV\ genomes}{infectious\ HdAd\ genomes\ /\ infectious\ RV\ genomes}$$

where Ad5-CMV-EGFP is RV, RV infectivity is VP/IU. IU is the average titer of end point dilution and transducing unit assays, HdAd vector genomes and RV genomes are the number of genomes from purified virus as determined by qPCR, and infectious HdAd genomes and infectious RV genomes are the number of genomes in DNA purified from coinfections.

HdAd $Ca_V2.1\ \alpha_1$ OE_mEGFP had a physical titer of $3.42*10^{12}$ VP/mL, and an infectious titer of $2.44*10^{11}$ IU/mL; 14:1 VP/IU. HdAd $Ca_V2.2\ \alpha_1$ OE_ mEGFP had a physical titer of $4.39*10^{12}$ VP/mL, and an infectious titer of $2.40*10^{11}$ IU/mL; 18:1 VP/IU.

Stereotaxic viral vector injections—HdAds were injected into the cochlear nucleus (CN) of C57BL/6J mice at postnatal day 1 (P1) using a stereotaxic injection approach (Chen et al., 2013). Briefly, P1 mice were anesthetized by hypothermia, using an ice bath for 5 min. Injection of 1.5 μL of HdAds expressing either $Ca_V2.1\ \alpha_1$ and EGFP, $Ca_V2.1\ \alpha_1$ and mEGFP, or $Ca_V2.2\ \alpha_1$ and mEGFP (~2.4×10^8 transducing units (TU)/μL) into the CN at a rate of 1 μL/min was performed using a glass needle (Blaubrand; IntraMARK). To dissipate the pressure, the needle was slowly removed two or three minutes after the injection. Afterwards, animals were placed under a warm lamp at ~37°C until fully recovered and were returned to their respective cages with their mothers.

For HdAd injections at P14, mice were anesthetized with 5% isoflurane inhalation and kept under 2% isoflurane throughout the procedure. Subcutaneous injection of physiological saline, lidocaine, bupivacaine and meloxicam was used to treat loss of liquid and alleviate pain. The fur on the scalp was removed chemically using hair remover lotion (Nair, Church & Dwight, UK). After cleaning and aseptic treatment with betadine and ethanol the skin was cut along the anterior-posterior axis. Injection site was determined using the Neurostar Stereodrive software (Neurostar) and corrected for head orientation and tilt. A small hole (diameter <1 mm) was drilled into the skull using a foot-pedal controlled drill MH-170 (Foredom). Virus solution identical to that used at P1 was injected via a 3.5" glass pipet (Drummond) at a rate of 100 nl/min with a nanoliter injector (NanoW, Neurostar) at 4 different positions, distance from lambda: (i) anterio-posterior (AP) –0.79, medio-lateral (ML) –2.34, dorso-ventral (DV) 5.4), (ii) AP –1.09, ML –2.34, DV5.4, (iii) AP –0.79, ML –2.44, DV 5.4, (iv) AP –1.09, ML-2.44, DV 5.4). After the injection, the skin was sutured, and the animal was kept under supervision until fully recovered. Afterwards it was returned to its mother.

Electrophysiology—During all experiments, slices were continuously perfused with standard aCSF at RT (~25°C) and visualized by an upright microscope (BX51WI, Olympus) through a 60x water-immersion objective (LUMPlanFL N, Olympus) and either CCD (QI-Click, QImaging) or EMCCD camera (Luca^{EM} S, Andor$^{™}$ Technology, Belfast, UK). Patch-clamp recordings were performed by using an EPC 10/2 patch-clamp amplifier, controlled by Patchmaster Software (HEKA, RRID:SCR 000034). Data were acquired at a sampling rate of 50 kHz and low-pass filtered at 6 kHz. To allow identification of calyces transduced

with HdAd expressing $Ca_V2.1$ α_1 OE or $Ca_V2.2$ α_1 OE, we co-expressed mEGFP as a marker. To visualize mEGFP, slices were illuminated at 470 nm wavelength using a Lumen 200 metal arc lamp (Prior Scientific) or a Polychrome V xenon bulb monochromator (ThermoFisher).

Preparation of acute slices—Acute brainstem slices were prepared as previously described (Chen et al., 2013). Briefly, after decapitation, the brains were immersed in ice-cold low-calcium artificial cerebrospinal fluid (aCSF, in mM): 125 NaCl, 2.5 KCl, 3 mM $MgCl_2$, 0.1 mM $CaCl_2$, 10 glucose, 25 $NaHCO_3$, 1.25 $NaHPO_4$, 0.4 L-ascorbic acid, 3 myo-inositol, and 2 Na-pyruvate, pH 7.3-7.4 (310 mOsmol). Coronal slices containing the MNTB were obtained using a vibrating tissue slicer (either Campden 7000 smz; Campden Instruments LTD or Leica VT1200; Leica Biosystems). Slices were immediately transferred to standard aCSF (37°C, continuously bubbled with 95% O_2-5% CO_2) containing the same as the low-calcium aCSF but with 1 mM $MgCl_2$ and 1-2 mM $CaCl_2$ (further specified below). After 45 min incubation, slices were transferred to a recording chamber with the same extracellular buffer at room temperature (RT: ~25°C).

Presynaptic recordings—To isolate presynaptic Ca^{2+} currents, the standard aCSF was supplemented with 1 μM tetrodotoxin (TTX; Tocris Bioscience), 100 μM 4-aminopyridin (4-AP; Tocris) and 20 mM tetraethylammonium chloride (TEA-Cl; Sigma Aldrich) to block Na^+ and K^+ channels. Calyces were whole-cell voltage clamped at −80 mV. Current-voltage relationships were recorded in the presence of 1 mM $MgCl_2$ and 1 mM $CaCl_2$, while pharmacological isolation of VGCC subtypes was performed in 2 mM $CaCl_2$. We used 200 nM ω-agatoxin IVA (Alomone labs) to selectively block $Ca_V2.1$ (P/Q-type) VGCCs and 2 μM ω-conotoxin GVIA (Alomone labs) for selective inhibition of $Ca_V2.2$ (N-type) VGCCs and supplemented 0.1 mg/mL cytochrome C to prevent toxin adsorption. All remaining Ca^{2+} channels were blocked by 50 μM $CdCl_2$. At P20/21 application of Cd^{2+} was not necessary because Ca^{2+} currents were completely blocked in presence of ω-agatoxin IVA and ω-conotoxin GVIA. Presynaptic patch pipettes were pulled to 4.5-6 MΩ and were filled with the following (in mM): 145 Cs-gluconate, 20 TEA-Cl, 10 HEPES, 2 Na_2-phosphocreatine, 4 MgATP, 0.3 NaGTP, and 0.5 EGTA, pH 7.2, 325-340 mOsmol). Sylgard coating was used to improve voltage-clamp quality. Presynaptic series resistance was between 6 and 25 MU (usually between 10-15 MΩ) and was compensated online to 6 MΩ with a time lag of 10 μs by the HEKA amplifier.

Afferent fiber stimulation—To trigger AP-evoked neurotransmitter release, we performed afferent fiber stimulation as previously described (Forsythe and Barnes-Davies, 1993). Briefly, a bipolar electrode (FHC Inc.) was placed halfway between the brainstem midline and MNTB. Recordings were performed in aCSF containing 1 mM $MgCl_2$ and 1.2 mM $CaCl_2$. Pipettes for postsynaptic recordings were pulled to a resistance of 2.5-4 MΩ and were filled with the same solution as presynaptic pipettes, but with 5 mM EGTA and 6 mM QX-314 (Sigma Aldrich). Postsynaptic MNTB principal neurons were voltage clamped to a holding potential of −60 mV. The standard aCSF was supplemented with 50 μM D-AP5 to block NMDA receptors (Tocris Bioscience), 20 μM bicuculline and 5 μM strychnine (Tocris Bioscience) to block inhibitory inputs. Furthermore, 0.25 mM (P7) or 1 mM (P20/21)

kynurenic acid (Tocris Bioscience) was added to avoid saturation of postsynaptic AMPA receptors. Postsynaptic R_s (<8 MΩ) was online compensated to R_s <3 MΩ. The remaining R_s was further compensated offline to 0 MΩ for all EPSCs with custom IgorPro routine (Traynelis, 1998).

Miniature postsynaptic currents (mEPSCs)—Miniature postsynaptic currents (mEPSCs) were recorded with 2 mM $CaCl_2$ in the aCSF. MNTB principal neurons were whole-cell voltage-clamped at −80 mV and aCSF was supplemented with 50 mM D-AP5, 20 mM bicuculline, 5 mM strychnine, 1 mM TTX and 20 mM TEA. For all recordings, series resistance was <8 MΩ and not compensated.

ELECTRON MICROSCOPY

Pre-embedding Immuno-Electron Microscopy—Wild type (C57BL/6J) and $Ca_V2.1$ $α_1$ OE injected mice, P7 and P21 were anesthetized with Tribromoethanol (250 mg/kg of body weight, i.p.) and perfused transcardially with phosphate-buffered saline (PBS, 150 mM NaCl, 25 mM Sørensen's phosphate buffer, pH 7.4) followed by fixative solution containing 4% paraformaldehyde (PFA), 0.1% or 0.5% glutaraldehyde, and 0.2% picric acid in 100mM Sørensen's phosphate buffer (PB, pH 7.4) for 7-9 min. Brains were post-fixed with 4% PFA in PB overnight and 50 μm coronal sections of the brainstem were obtained on a vibratome (Leica VT1200). Expression of EGFP at calyx of Held terminals was visualized using an epifluorescence inverted microscope (CKX41, Olympus) equipped with an XCite Series 120Q lamp (Excelitas technologies), and only EGFP positive samples were further processed as previously reported (Montesinos et al., 2015). After washing with PB, sections were cryoprotected with 10%, 20% and 30% sucrose in PB and submersed into liquid nitrogen for permeabilization, then thawed. Then sections were incubated in a blocking solution containing 10% normal goat serum (NGS), 1% fish skin gelatin (FSG), in 50 mM Tris-buffered saline (TBS, 150 mM NaCl, 50 mM Tris, pH 7.4) for 1h, and incubated with an anti-GFP antibody (0.1 μg/mL, Abcam, cat# ab6556, RRID:AB_305564) diluted in TBS containing 1% NGS, 0.1% FSG plus 0.05% NaN_3 at 4°C for 48h. After washing with TBS, sections were incubated overnight in nanogold conjugated goat anti-rabbit IgG (1:100, Nanoprobes, Cat# 2003) diluted in TBS containing 1% NGS and 0.1% FSG. Immunogold-labeled sections were washed in PBS, briefly fixed with 1% glutaraldehyde in PBS, and silver intensified using HQ silver intensification kit (Nanoprobe). After washing with PB, they were treated with 0.5% OsO_4 in 0.1M PB for 20 min, en-bloc stained with 1% uranyl acetate, dehydrated and flat embedded in Durcupan resin (Sigma-Aldrich). After trimming out the MNTB region, ultrathin sections were prepared with 40 nm-thickness using an ultramicrotome (EM UC7, Leica). Sections were counterstained with uranyl acetate and lead citrate, and examined in a Tecnai G2 Spirit Bio-Twin transmission electron microscope (Thermo Fisher Scientific) at 100kV acceleration voltage. Images were taken with a Veleta CCD camera (Olympus) operated by TIA software (FEI). Images used for quantification were taken at 60,000x magnification.

SDS-digested freeze fracture replica immunogold labeling—$Ca_V2.1$ $α_1$ OE-injected mice harboring myristoylated EGFP were anesthetized with tribromoethanol (250 mg/kg of body weight, i.p.) and perfused transcardially with PBS followed by 2% PFA, and

0.2% picric acid in 0.1M PB for 12 min. 130 μm-thick coronal sections of brainstem were obtained using a vibratome (Leica VT1200). Only those samples showing mEGFP expression were selected. The brain slices containing the MNTB region were cryoprotected in 10%, 20% for 30 min each and 30% glycerol at 4°C overnight. Small pieces containing MNTB region were trimmed out and frozen using a high pressure freezing machine (HPM100, Leica). Frozen samples were fractured in two halves using a double replication device at –120°C, replicated first with a 2 nm carbon deposition, shadowed from 60 degree angle by carbon-platinum of 2 nm and supported by a final carbon deposition of 20-30nm, using a JFDV Freeze fracture machine (JEOL/Boeckeler). The tissue was dissolved by placing the replicas in a digesting solution containing 2.5% SDS, 20% sucrose and 15mM Tris-HCl (pH8.3) with gentle agitation in an oven at 82.5°C for 18 hours. The replicas were washed and blocked with 4% BSA and 1% FSG in TBS for 1 hour, then incubated with a mixture of primary antibody; rabbit anti- GFP (1 μg/mL, AbCam cat#ab6556, RRID:AB_305564) and guinea pig anti-Ca$_V$2.1 α$_1$ subunit (0.7 μg/mL, Synaptic Systems cat# 152205, RRI-D:AB_2619842) diluted in 0.04% BSA and 0.01% FSG in TBS for 18 h at room temperature. After several washes, the replicas were incubated in donkey anti-rabbit IgG conjugated to 6 nm gold particles and donkey anti-guinea pig IgG conjugated to 12 nm gold particles (1:30; Jackson ImmunoResearch; RRID:AB_2340585 and RRID:AB_2340465) diluted in 0.04% BSA and 0.01% FSG in TBS for 18 h at room temperature. After being washed, the replicas were picked up on 100-parallel-bar copper grids or aperture grids and examined with a Tecnai G2 Spirit BioTwin transmission electron microscope (Thermo Fisher Scientific) at 100 kV acceleration voltage. Images were taken with a Veleta CCD camera (Olympus).

QUANTIFICATION AND STATISTICAL ANALYSIS

Electrophysiological data analysis—All data were analyzed offline with Fitmaster (Harvard Instruments, RRID:SCR_016233) and custom routines in Matlab (version 9.3; Mathworks, RRID:SCR_001622) or IgorPro (version 6.37, Wavemetrics, RRID:SCR_000325) equipped with Patcher's Power Tools (version 2.19, RRID:SCR_001950). Voltage-dependence of Ca^{2+} channel activation was described by peak of the steady state current as well as tail currents as functions of voltage. Peak currents were fitted with an IgorPro routine according to a Hodgkin-Huxley formalism with four independent gates assuming a Goldman-Hodgkin-Katz (GHK) open-channel conductance $\Gamma(V)$ as function of voltage:

$$I(V) = \Gamma(V)\frac{1 - e^{-\frac{V - E_{rev}}{25\,mV}}}{1 - e^{-\frac{V}{25\,mV}}} \cdot \frac{1}{\left(1 - e^{\frac{V - V_m}{k_m}}\right)^4} \quad (1)$$

with E_{rev} as reversal potential, V_m as half-maximal activation voltage per gate, and k_m as the voltage-dependence of activation. Tail currents were measured as peaks minus baseline and fitted with an IgorPro routine according to a Boltzmann formalism:

$$I_{tail} = I_{base} + \frac{I_{min}}{1 + e^{-\frac{V - V_{0.5}}{k}}} \quad (2)$$

with $V_{0.5}$ as half-maximal activation voltage and k voltage-dependence of activation. EPSCs were measured as peak minus baseline preceding the EPSC.

Miniature EPSCs (mEPSCs) were analyzed using a custom written script in IgorPro provided by H. Taschenberger based on (Clements and Bekkers, 1997). All events were manually curated and non-linear least-square fit with a multi-exponential equation of the form:

$$A(1 - e^{-t/\tau_r})(Fe^{-t/\tau_{d1}} + (1 - F)e^{-t/\tau_{d2}}) \quad (3)$$

Fitting of the events was performed in Matlab using the Trust-Region-Reflective fitting algorithm and mEPSC amplitudes were derived from the fit. Overlapping events were first deconvolved with a template mEPSC to determine their onset and then fit as a linear sum of multi-exponential equations.

Readily-releasable pool (RRP) approximations—The afferent fiber stimulation data were used to determine the RRP with a back-extrapolation method (SMN, (Neher, 2015; Schneggenburger et al., 1999). Briefly, the cumulative EPSC amplitude vs. stimulus number was plotted and then back extrapolated with a line fit from the steady state increase of cumulative EPSC amplitudes. To account for the underestimation in pool sizes due to incomplete pool depletion we applied a correction method assuming no change in P_r throughout the train ($p_0/p_n = 1$) and no replenishment between 1st and 2nd pulse (Neher, 2015). Release probability was calculated by dividing the first EPSC by the respective RRP. Additionally, a pool depletion model (NpRf model, (Thanawala and Regehr, 2016) was used to fit EPSCs using the Trust-Region-Reflective fitting algorithm with N0 (initial RRP size), p0 (initial release probability) and R (replenishment rate) being constrained to positive values. For the NpRf model, P_r was determined during the fit and defined as $EPSC_0/N_0$.

TEM image analysis for active zone length and synaptic vesicle numbers—We identified calyces which were positive for EGFP expression by immunogold labeling with an anti-GFP antibody and compared EGFP-positive terminals ($Ca_V2.1$ α_1 OE) to EGFP-negative terminals (control) in the same slice. All TEM data were analyzed using Fiji imaging analysis software (RRID:SCR_002285, http://fiji.sc)(Schindelin et al., 2012). Each presynaptic active zone (AZ) was defined as the membrane directly opposing postsynaptic density, and the length of each AZ was measured. Vesicles within 200 nm of each AZ were manually selected and their distances relative to the AZ were calculated using a 32-bit

Euclidean distance map generated from the AZ. For data analysis, vesicle distances were binned every 5 nm and counted. Vesicles less than 5 nm from the AZ were considered "docked" (Taschenberger et al., 2002). At least three animals for each condition and 40 AZs per animal were analyzed.

Replica image collection and analysis—Presynaptic P-faces (protoplasmic face of the cell membrane) of the calyx of Held were morphologically identified by existence of cross-fractured cytoplasm containing synaptic vesicles and/or by existence of glutamate receptor clusters uniquely shown on the adjacent E-face (exoplasmic face) of the postsynaptic cell of principle neuron of MNTB (Budisantoso et al., 2012; Nakamura et al., 2015). Specifically, immunogold-labeled presynaptic P-faces that were in contact with the postsynaptic soma were imaged at 43,000x magnification. mEGFP-positive presynaptic P-faces were identified by the existence of 6 nm immunogold particles as $Ca_V2.1$ α_1 OE terminals, and mEGFP-negative calyx terminals were categorized as control. We analyzed the distribution and number of $Ca_V2.1$ from the 12 nm immunogold labeling in both mEGFP positive and negative terminals. Between seven and thirteen individual P-faces, including small to large pieces, were analyzed for each condition, comprising 50-165 μm^2 of P-face area respectively. For each continuous P-face, images were manually stitched and minimally adjusted for brightness and contrast (Adobe Photoshop CS6), and 12 nm gold particles corresponding to $Ca_V2.1$ channels were thresholded and quantified using Microscopy Image Browser (RRID:SCR_016560(Belevich et al., 2016). A custom macro was used in Fiji to extend a circle with a 30nm and a 100 nm radius from each 12 nm gold particle to form clusters of closely distributed $Ca_V2.1$ channels (Althof et al., 2015; Nakamura et al., 2015). Cluster size and the number of particles within clusters were then analyzed. The parameters "Gold particle # per cluster", "Cluster area" and "Gold particle density per cluster area" are derived from the 30 nm analysis. The parameters "Gold particle density per putative AZ" and "Putative AZ area" derived from the 100 nm analysis. By combining both the 30 nm and 100 nm analyses we derived "Cluster number per putative AZ" defined as all 30 nm clusters within 100 nm radius and "single Gold particles per putative AZ" which correspond to all single particles within 100 nm radius/AZ. The nearest neighbor distance of $Ca_V2.1$ channels was calculated as the minimal Euclidean distance of each gold particle to all other gold particles within the same cluster.

STATISTICAL ANALYSIS

Statistical tests were conducted in Prism 7 (RRID:SCR_002798, GraphPad Software) and Matlab. All data were tested for normal distribution by performing a Shapiro-Wilk test for normality and variances of all data were estimated and compared using Levene's test. To account for unequal variance between two groups, t test with Welch's correction was applied. In case of unequal variance between three groups, Mood's median test with a *post hoc* Bonferroni test was performed. Electrophysiological data were compared with unpaired t test or Mann-Whitney U test when comparing two groups and Kruskal-Wallis test with a *post hoc* Dunn's test, when comparing more than two groups using the control dataset for comparison. Since our hypothesis was that $Ca_V2.1$ α_1 OE increased $Ca_V2.1$ levels at the AZ, one-tailed tests were used for comparing I_{Ca} and $Ca_V2.1$ numbers and clusters. Patch clamp recordings lacking proper clamp quality or with high leak (>100 pA presynaptic, >200 pA

postsynaptic) were excluded from data sets. Only EPSC trains without failures were used to quantify RRP size and P_r. EM data were compared using unpaired t test or Mann-Whitney U test. The contingency of the distribution of clustered and single nanogold particles in SDS-FFRL data were assessed with Fisher's exact test. No statistical methods were used to predetermine sample size. Statistical significance was accepted at * $P<0.05$; ** $P<0.01$; *** $P<0.001$; **** $P<0.0001$. In figures and tables, data are reported as mean ± SEM, unless otherwise stated.

Supplementary Material

Refer to Web version on PubMed Central for supplementary material.

REFERENCES

Althof D, Baehrens D, Watanabe M, Suzuki N, Fakler B, and Kulik Á (2015). Inhibitory and excitatory axon terminals share a common nano-architecture of their Cav2.1 (P/Q-type) Ca(2+) channels. Front. Cell. Neurosci. 9, 315. [PubMed: 26321916]

Ariel P, Hoppa MB, and Ryan TA (2013). Intrinsic variability in Pv, RRP size, Ca(2+) channel repertoire, and presynaptic potentiation in individual synaptic boutons. Front. Synaptic Neurosci. 4, 9. [PubMed: 23335896]

Basu J, Betz A, Brose N, and Rosenmund C (2007). Munc13-1 C1 domain activation lowers the energy barrier for synaptic vesicle fusion. J. Neurosci. 27, 1200–1210. [PubMed: 17267576]

Baur D, Bornschein G, Althof D, Watanabe M, Kulik A, Eilers J, and Schmidt H (2015). Developmental tightening of cerebellar cortical synaptic influx-release coupling. J. Neurosci. 35, 1858–1871. [PubMed: 25653347]

Belevich I, Joensuu M, Kumar D, Vihinen H, and Jokitalo E (2016). Microscopy Image Browser: a platform for segmentation and analysis of multidimensional datasets. PLoS Biol. 14, e1002340. [PubMed: 26727152]

Bewig B, and Schmidt WE (2000). Accelerated titering of adenoviruses. Biotechniques 28, 870–873. [PubMed: 10818691]

Bollmann JH, Sakmann B, and Borst JG (2000). Calcium sensitivity of glutamate release in a calyx-type terminal. Science 289, 953–957. [PubMed: 10937999]

Borst JG, and Soria van Hoeve J (2012). The calyx of Held synapse: from model synapse to auditory relay. Annu. Rev. Physiol. 74, 199–224. [PubMed: 22035348]

Bucurenciu I, Bischofberger J, and Jonas P (2010).A small number of open Ca2+ channels trigger transmitter release at a central GABAergic synapse. Nat. Neurosci. 13, 19–21. [PubMed: 20010820]

Budisantoso T, Matsui K, Kamasawa N, Fukazawa Y, and Shigemoto R (2012). Mechanisms underlying signal filtering at a multisynapse contact. J. Neurosci. 32, 2357–2376. [PubMed: 22396411]

Cao YQ, and Tsien RW (2010). Different relationship of N- and P/Q-type Ca2+ channels to channel-interacting slots in controlling neurotransmission at cultured hippocampal synapses. J. Neurosci. 30, 4536–4546. [PubMed: 20357104]

Cao YQ, Piedras-Rentería ES, Smith GB, Chen G, Harata NC, and Tsien RW (2004). Presynaptic Ca2+ channels compete for channel type-preferring slots in altered neurotransmission arising from Ca2+ channelopathy. Neuron 43, 387–400. [PubMed: 15294146]

Catterall WA (2011). Voltage-gated calcium channels. Cold Spring Harb. Perspect. Biol. 3, a003947. [PubMed: 21746798]

Chen Z, Cooper B, Kalla S, Varoqueaux F, and Young SM, Jr. (2013). The Munc13 proteins differentially regulate readily releasable pool dynamics and calcium-dependent recovery at a central synapse. J. Neurosci. 33, 8336–8351. [PubMed: 23658173]

Chen Z, Das B, Nakamura Y, DiGregorio DA, and Young SM, Jr. (2015). Ca2+ channel to synaptic vesicle distance accounts for the readily releasable pool kinetics at a functionally mature auditory synapse. J. Neurosci. 35, 2083–2100. [PubMed: 25653365]

Clarke GL, Chen J, and Nishimune H (2012). Presynaptic active zone density during development and synaptic plasticity. Front. Mol. Neurosci. 5, 12. [PubMed: 22438837]

Clements JD, and Bekkers JM (1997). Detection of spontaneous synaptic events with an optimally scaled template. Biophys. J. 73, 220–229. [PubMed: 9199786]

Davis GW, and Müller M (2015). Homeostatic control of presynaptic neurotransmitter release. Annu. Rev. Physiol. 77, 251–270. [PubMed: 25386989]

Davydova D, Marini C, King C, Klueva J, Bischof F, Romorini S, Montenegro-Venegas C, Heine M, Schneider R, Schröder MS, et al. (2014). Bassoon specifically controls presynaptic P/Q-type Ca(2+) channels via RIM-binding protein. Neuron 82, 181–194. [PubMed: 24698275]

Dong W, Radulovic T, Goral RO, Thomas C, Suarez Montesinos M, Guerrero-Given D, Hagiwara A, Putzke T, Hida Y, Abe M, et al. (2018). CAST/ELKS proteins control voltage-gated Ca(2+) channel density and synaptic release probability at a mammalian central synapse. Cell Rep. 24, 284–293. [PubMed: 29996090]

Doughty JM, Barnes-Davies M, Rusznák Z, Harasztosi C, and Forsythe ID (1998). Contrasting Ca2+ channel subtypes at cell bodies and synaptic terminals of rat anterioventral cochlear bushy neurones. J. Physiol. 512, 365–376. [PubMed: 9763627]

Eggermann E, Bucurenciu I, Goswami SP, and Jonas P (2011). Nanodomain coupling between Ca^{2+} channels and sensors of exocytosis at fast mammalian synapses. Nat. Rev. Neurosci. 13, 7–21. [PubMed: 22183436]

Fedchyshyn MJ, and Wang LY (2005). Developmental transformation of the release modality at the calyx of Held synapse. J. Neurosci. 25, 4131–4140. [PubMed: 15843616]

Felix R, and Weiss N (2017). Ubiquitination and proteasome-mediated degradation of voltage-gated Ca2+ channels and potential pathophysiological implications. Gen. Physiol. Biophys. 36, 1–5. [PubMed: 27787228]

Forsythe ID, and Barnes-Davies M (1993). The binaural auditory pathway: membrane currents limiting multiple action potential generation in the rat medial nucleus of the trapezoid body. Proc. Biol. Sci. 251, 143–150. [PubMed: 8096080]

Fouquet W, Owald D, Wichmann C, Mertel S, Depner H, Dyba M, Hallermann S, Kittel RJ, Eimer S, and Sigrist SJ (2009). Maturation of active zone assembly by Drosophila Bruchpilot. J. Cell Biol. 186, 129–145. [PubMed: 19596851]

Hagiwara A, Fukazawa Y, Deguchi-Tawarada M, Ohtsuka T, and Shigemoto R (2005). Differential distribution of release-related proteins in the hippocampal CA3 area as revealed by freeze-fracture replica labeling. J. Comp. Neurol. 489, 195–216. [PubMed: 15983999]

Han Y, Kaeser PS, Südhof TC, and Schneggenburger R (2011). RIM determines Ca^{2+} channel density and vesicle docking at the presynaptic active zone. Neuron 69, 304–316. [PubMed: 21262468]

Hefft S, and Jonas P (2005). Asynchronous GABA release generates long-lasting inhibition at a hippocampal interneuron-principal neuron synapse. Nat. Neurosci. 8, 1319–1328. [PubMed: 16158066]

Holderith N, Lorincz A, Katona G, Rózsa B, Kulik A, Watanabe M, and Nusser Z (2012). Release probability of hippocampal glutamatergic terminals scales with the size of the active zone. Nat. Neurosci. 15, 988–997. [PubMed: 22683683]

Hoppa MB, Lana B, Margas W, Dolphin AC, and Ryan TA (2012). α2δ expression sets presynaptic calcium channel abundance and release probability. Nature 486, 122–125. [PubMed: 22678293]

Inchauspe CG, Martini FJ, Forsythe ID, and Uchitel OD (2004). Functional compensation of P/Q by N-type channels blocks short-term plasticity at the calyx of Held presynaptic terminal. J. Neurosci. 24, 10379–10383. [PubMed: 15548652]

Indriati DW, Kamasawa N, Matsui K, Meredith AL, Watanabe M, and Shigemoto R (2013). Quantitative localization of Cav2.1 (P/Q-type) voltage-dependent calcium channels in Purkinje cells: somatodendritic gradient and distinct somatic coclustering with calcium-activated potassium channels. J. Neurosci. 33, 3668–3678. [PubMed: 23426693]

Iwasaki S, and Takahashi T (1998). Developmental changes in calcium channel types mediating synaptic transmission in rat auditory brainstem. J. Physiol. 509, 419–423. [PubMed: 9575291]

Iwasaki S, and Takahashi T (2001). Developmental regulation of transmitter release at the calyx of Held in rat auditory brainstem. J. Physiol. 534, 861–871. [PubMed: 11483715]

Iwasaki S, Momiyama A, Uchitel OD, and Takahashi T (2000). Developmental changes in calcium channel types mediating central synaptic transmission. J. Neurosci. 20, 59–65. [PubMed: 10627581]

Kaeser PS, Deng L, Wang Y, Dulubova I, Liu X, Rizo J, and Südhof TC (2011). RIM proteins tether Ca2+ channels to presynaptic active zones via a direct PDZ-domain interaction. Cell 144, 282–295. [PubMed: 21241895]

Kittel RJ, Wichmann C, Rasse TM, Fouquet W, Schmidt M, Schmid A, Wagh DA, Pawlu C, Kellner RR, Willig KI, et al. (2006). Bruchpilot promotes active zone assembly, Ca2+ channel clustering, and vesicle release. Science 312, 1051–1054. [PubMed: 16614170]

Lenkey N, Kirizs T, Holderith N, Máté Z, Szabó G, Vizi ES, Hájos N, and Nusser Z (2015). Tonic endocannabinoid-mediated modulation of GABA release is independent of the CB1 content of axon terminals. Nat. Commun. 6, 6557. [PubMed: 25891347]

Lipscombe D, Andrade A, and Allen SE (2013). Alternative splicing: functional diversity among voltage-gated calcium channels and behavioral consequences. Biochim. Biophys. Acta 1828, 1522–1529. [PubMed: 23022282]

Lorteije JA, Rusu SI, Kushmerick C, and Borst JG (2009). Reliability and precision of the mouse calyx of Held synapse. J. Neurosci. 29, 13770–13784. [PubMed: 19889989]

Lübbert M, Goral RO, Satterfield R, Putzke T, van den Maagdenberg AM, Kamasawa N, and Young SM, Jr. (2017). A novel region in the $Ca_V2.1$ α_1 subunit C-terminus regulates fast synaptic vesicle fusion and vesicle docking at the mammalian presynaptic active zone. eLife 6, e28412. [PubMed: 28786379]

Mallmann RT, Elgueta C, Sleman F, Castonguay J, Wilmes T, van den Maagdenberg A, and Klugbauer N (2013). Ablation of Ca(V)2.1 voltagegated Ca^{2+} channels in mouse forebrain generates multiple cognitive impairments. PLoS ONE 8, e78598. [PubMed: 24205277]

Maschi D, and Klyachko VA (2017). Spatiotemporal regulation of synaptic vesicle fusion sites in central synapses. Neuron 94, 65–73. [PubMed: 28343869]

Miki T, Hirai H, and Takahashi T (2013). Activity-dependent neurotrophin signaling underlies developmental switch of Ca2+ channel subtypes mediating neurotransmitter release. J. Neurosci. 33, 18755–18763. [PubMed: 24285882]

Miki T, Kaufmann WA, Malagon G, Gomez L, Tabuchi K, Watanabe M, Shigemoto R, and Marty A (2017). Numbers of presynaptic Ca^{2+} channel clusters match those of functionally defined vesicular docking sites in single central synapses. Proc. Natl. Acad. Sci. USA 114, E5246–E5255. [PubMed: 28607047]

Momiyama T (2003). Parallel decrease in omega-conotoxin-sensitive transmission and dopamine-induced inhibition at the striatal synapse of developing rats. J. Physiol. 546, 483–490. [PubMed: 12527734]

Montesinos MS, Chen Z, and Young SM, Jr. (2011). pUNISHER: a high-level expression cassette for use with recombinant viral vectors for rapid and long term in vivo neuronal expression in the CNS. J. Neurophysiol. 106, 3230–3244. [PubMed: 21957229]

Montesinos MS, Dong W, Goff K, Das B, Guerrero-Given D, Schmalzigaug R, Premont RT, Satterfield R, Kamasawa N, and Young SM, Jr. (2015). Presynaptic deletion of GIT proteins results in increased synaptic strength at a mammalian central synapse. Neuron 88, 918–925. [PubMed: 26637799]

Montesinos MS, Satterfield R, and Young SM, Jr. (2016). Helper-dependent adenoviral vectors and their use for neuroscience applications. Methods Mol. Biol. 1474, 73–90. [PubMed: 27515075]

Müller CS, Haupt A, Bildl W, Schindler J, Knaus HG, Meissner M, Rammner B, Striessnig J, Flockerzi V, Fakler B, and Schulte U (2010). Quantitative proteomics of the Cav2 channel nano-environments in the mammalian brain. Proc. Natl. Acad. Sci. USA 107, 14950–14957. [PubMed: 20668236]

Müller M, Liu KS, Sigrist SJ, and Davis GW (2012). RIM controls homeostatic plasticity through modulation of the readily-releasable vesicle pool. J. Neurosci. 32, 16574–16585. [PubMed: 23175813]

Nakamura Y, Harada H, Kamasawa N, Matsui K, Rothman JS, Shigemoto R, Silver RA, DiGregorio DA, and Takahashi T (2015). Nanoscale distribution of presynaptic Ca(2+) channels and its impact on vesicular release during development. Neuron 85, 145–158. [PubMed: 25533484]

Neher E (2010). What is rate-limiting during sustained synaptic activity: vesicle supply or the availability of release sites. Front. Synaptic Neurosci. 2, 144. [PubMed: 21423530]

Neher E (2015). Merits and limitations of vesicle pool models in view of heterogeneous populations of synaptic vesicles. Neuron 87, 1131–1142. [PubMed: 26402599]

Nusser Z (2018). Creating diverse synapses from the same molecules. Curr. Opin. Neurobiol. 51, 8–15. [PubMed: 29353084]

Palmer D, and Ng P (2003). Improved system for helper-dependent adenoviral vector production. Mol. Ther. 8, 846–852. [PubMed: 14599819]

Palmer DJ, and Ng P (2011). Rescue, amplification, and large-scale production of helper-dependent adenoviral vectors. Cold Spring Harb. Protoc. 2011, 857–866. [PubMed: 21724821]

Parthier D, Kuner T, and Körber C (2018). The presynaptic scaffolding protein Piccolo organizes the readily releasable pool at the calyx of Held. J. Physiol. 596, 1485–1499. [PubMed: 29194628]

Puntel M, Curtin JF, Zirger JM, Muhammad AK, Xiong W, Liu C, Hu J, Kroeger KM, Czer P, Sciascia S, et al. (2006). Quantification of high-capacity helper-dependent adenoviral vector genomes in vitro and in vivo, using quantitative TaqMan real-time polymerase chain reaction. Hum. Gene Ther. 17, 531–544. [PubMed: 16716110]

Rollenhagen A, Sätzler K, Rodríguez EP, Jonas P, Frotscher M, and Lübke JH (2007). Structural determinants of transmission at large hippocampal mossy fiber synapses. J. Neurosci. 27, 10434–10444. [PubMed: 17898215]

Sakamoto H, Ariyoshi T, Kimpara N, Sugao K, Taiko I, Takikawa K, Asanuma D, Namiki S, and Hirose K (2018). Synaptic weight set by Munc13-1 supramolecular assemblies. Nat. Neurosci. 21, 41–49. [PubMed: 29230050]

Sätzler K, Söhl LF, Bollmann JH, Borst JG, Frotscher M, Sakmann B, and Lübke JH (2002). Three-dimensional reconstruction of a calyx of Held and its postsynaptic principal neuron in the medial nucleus of the trapezoid body. J. Neurosci. 22, 10567–10579. [PubMed: 12486149]

Schikorski T, and Stevens CF (2001). Morphological correlates of functionally defined synaptic vesicle populations. Nat. Neurosci. 4, 391–395. [PubMed: 11276229]

Schindelin J, Arganda-Carreras I, Frise E, Kaynig V, Longair M, Pietzsch T, Preibisch S, Rueden C, Saalfeld S, Schmid B, et al. (2012). Fiji: an open-source platform for biological-image analysis. Nat. Methods 9, 676–682. [PubMed: 22743772]

Schneggenburger R, and Neher E (2000). Intracellular calcium dependence of transmitter release rates at a fast central synapse. Nature 406, 889–893. [PubMed: 10972290]

Schneggenburger R, and Rosenmund C (2015). Molecular mechanisms governing Ca(2+) regulation of evoked and spontaneous release. Nat. Neurosci. 18, 935–941. [PubMed: 26108721]

Schneggenburger R, Meyer AC, and Neher E (1999). Released fraction and total size of a pool of immediately available transmitter quanta at a calyx synapse. Neuron 23, 399–409. [PubMed: 10399944]

Schneider R, Hosy E, Kohl J, Klueva J, Choquet D, Thomas U, Voigt A, and Heine M (2015). Mobility of calcium channels in the presynaptic membrane. Neuron 86, 672–679. [PubMed: 25892305]

Scholz KP, and Miller RJ (1995). Developmental changes in presynaptic calcium channels coupled to glutamate release in cultured rat hippocampal neurons. J. Neurosci. 15, 4612–4617. [PubMed: 7790927]

Sheng J, He L, Zheng H, Xue L, Luo F, Shin W, Sun T, Kuner T, Yue DT, and Wu LG (2012). Calcium-channel number critically influences synaptic strength and plasticity at the active zone. Nat. Neurosci. 15, 998–1006. [PubMed: 22683682]

Siksou L, Rostaing P, Lechaire JP, Boudier T, Ohtsuka T, Fejtová A, Kao HT, Greengard P, Gundelfinger ED, Triller A, and Marty S (2007). Three-dimensional architecture of presynaptic terminal cytomatrix. J. Neurosci. 27, 6868–6877. [PubMed: 17596435]

Simms BA, and Zamponi GW (2014). Neuronal voltage-gated calcium channels: structure, function, and dysfunction. Neuron 82, 24–45. [PubMed: 24698266]

Smith JE, and Reese TS (1980). Use of aldehyde fixatives to determine the rate of synaptic transmitter release. J. Exp. Biol. 89, 19–29. [PubMed: 6110693]

Sonntag M, Englitz B, Kopp-Scheinpflug C, and Rübsamen R (2009). Early postnatal development of spontaneous and acoustically evoked discharge activity of principal cells of the medial nucleus of the trapezoid body: an in vivo study in mice. J. Neurosci. 29, 9510–9520. [PubMed: 19641114]

Sonntag M, Englitz B, Typlt M, and Rübsamen R (2011). The calyx of Held develops adult-like dynamics and reliability by hearing onset in the mouse in vivo. J. Neurosci. 31, 6699–6709. [PubMed: 21543599]

Stanley EF (2016). The Nanophysiology of Fast Transmitter Release. Trends Neurosci. 39, 183–197. [PubMed: 26896416]

Takahashi T, and Momiyama A (1993). Different types of calcium channels mediate central synaptic transmission. Nature 366, 156–158. [PubMed: 7901765]

Taschenberger H, Leão RM, Rowland KC, Spirou GA, and von Gersdorff H (2002). Optimizing synaptic architecture and efficiency for high-frequency transmission. Neuron 36, 1127–1143. [PubMed: 12495627]

Thanawala MS, and Regehr WG (2013). Presynaptic calcium influx controls neurotransmitter release in part by regulating the effective size of the readily releasable pool. J. Neurosci. 33, 4625–4633. [PubMed: 23486937]

Thanawala MS, and Regehr WG (2016). Determining synaptic parameters using high-frequency activation. J. Neurosci. Methods 264, 136–152. [PubMed: 26972952]

Traynelis SF (1998). Software-based correction of single compartment series resistance errors. J. Neurosci. Methods 86, 25–34. [PubMed: 9894783]

Wheeler DB, Randall A, and Tsien RW (1994). Roles of N-type and Q-type Ca2+ channels in supporting hippocampal synaptic transmission. Science 264, 107–111. [PubMed: 7832825]

Wu LG, Borst JG, and Sakmann B (1998). R-type Ca2+ currents evoke transmitter release at a rat central synapse. Proc. Natl. Acad. Sci. USA 95, 4720–4725. [PubMed: 9539805]

Wu LG, Westenbroek RE, Borst JG, Catterall WA, and Sakmann B (1999). Calcium channel types with distinct presynaptic localization couple differentially to transmitter release in single calyx-type synapses. J. Neurosci. 19, 726–736. [PubMed: 9880593]

Young SM, Jr., and Neher E (2009). Synaptotagmin has an essential function in synaptic vesicle positioning for synchronous release in addition to its role as a calcium sensor. Neuron 63, 482–496. [PubMed: 19709630]

Highlights

- $Ca_V2.1$ dominate presynaptic active zones are not fully occupied by $Ca_V2.1$ channels

- Presynaptic $Ca_V2.1$ channel numbers can increase regardless of developmental state

- Higher synaptic vesicle release probability with increased $Ca_V2.1$ channel numbers

- $Ca_V2.1$ completely competes away $Ca_V2.2$ channels, but not vice versa

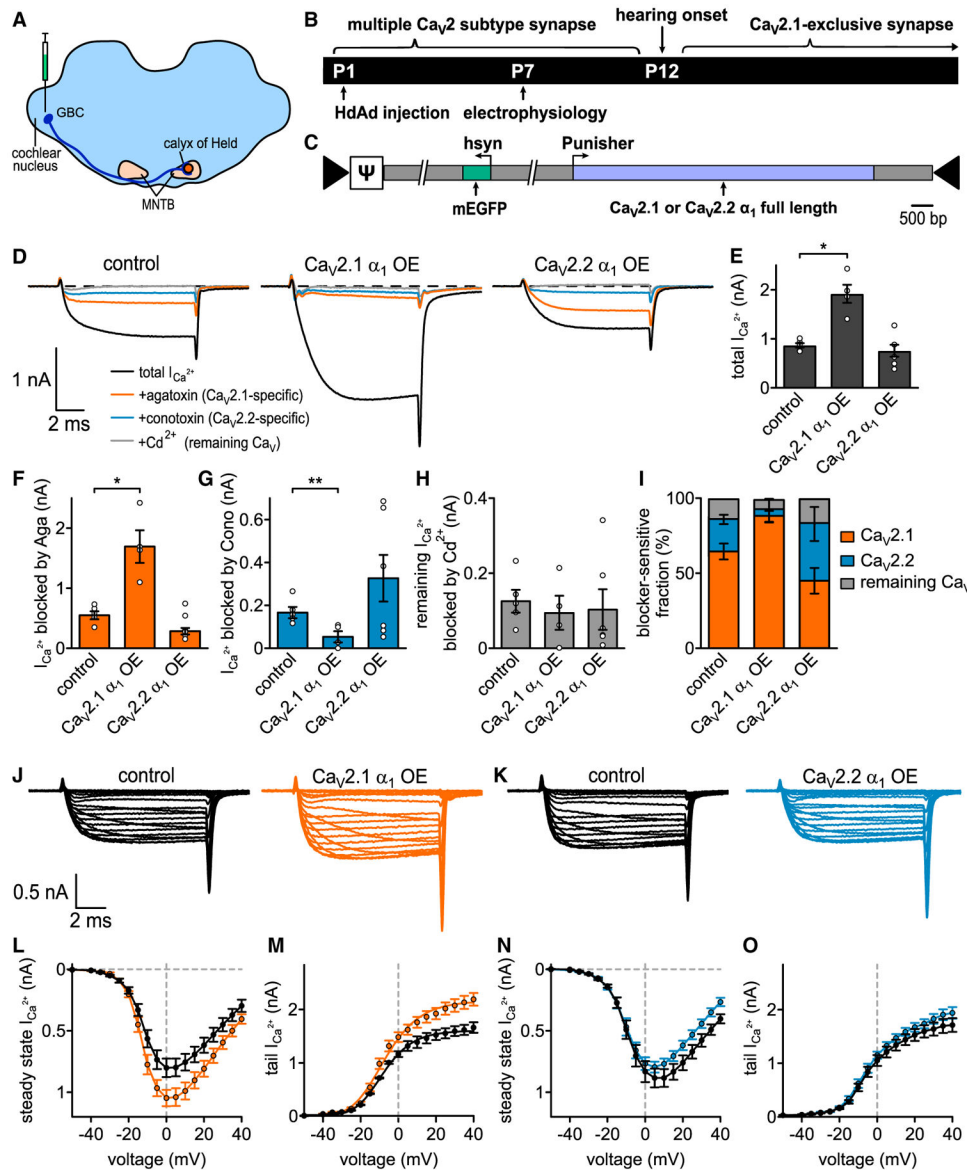**Figure 1. Ca$_V$2.1 α$_1$ OE Results in Increased Ca$_V$2.1 Currents and Almost Complete Loss of Ca$_V$2.2 Currents at the P7 Calyx**

(A) Schematic of auditory brainstem. Globular bushy cells (GBC) which give rise to the calyx of Held are depicted for clarity.

(B) (Top) Developmental transition of calyx of Held from multiple Ca$_V$2 subtype synapse to Ca$_V$2 exclusive at onset of hearing (P12). (Bottom) Experimental timeline from virus injection into VCN at P1 to electrophysiological recordings at P7.

(C) Schematic of HdAd constructs expressing either Ca$_V$2.1 or Ca$_V$2.2 cDNAs (light blue) driven by the Punisher overexpression cassette and mEGFP marker (green) driven by a 470 bp human synapsin promoter; arrows indicate viral inverted terminal repeat sequences; J indicates the viral genome packaging signal sequence.

(D) Pharmacological isolation of Ca$_V$2 isoforms expressed in the presynaptic terminal at P7 in control (n = 5), Ca$_V$2.1 α$_1$ OE (n = 4), or Ca$_V$2.2 α$_1$ OE (n = 6). Average traces before

application of blockers (black), after applying 200 nM ω-agatoxin IVA to specifically block $Ca_V2.1$ (Aga, brown), after 2 μM ω-conotoxin GVIA to block $Ca_V2.2$ (Cono, blue) and 50 μM Cd^{2+} to block the remaining Ca^{2+} currents (gray).

(E–H) Ca^{2+} current amplitudes before blocker application ($Ca_V2.1$ α_1 OE versus control, p = 0.0328 Mood's median test and *post hoc* Bonferroni test), Aga-sensitive Ca^{2+} current amplitudes ($Ca_V2.1$ α_1 OE versus control, p = 0.0328), Cono-sensitive Ca^{2+} current amplitudes ($Ca_V2.1$ α_1 OE versus control, p = 0.0054), and Cd^{2+}-sensitive Ca^{2+} current amplitudes (n.s., Kruskal Wallis and *post hoc* Dunn's test, n = 5/4/6 for control, $Ca_V2.1$ α_1 OE, and $Ca_V2.2$ α_1 OE, respectively).

(I) Relative Ca^{2+} current fractions sensitive to respective blockers.

(J and K) Average Ca^{2+} current traces to 10 ms step depolarizations from −80 mV holding to voltages between −50 and +40 mV for control (J and K, left, black) and $Ca_V2.1$ α_1 OE (J, right, brown) or $Ca_V2.2$ α_1 OE (K, right, blue).

(L–O) Current-voltage relationships of either steady-state Ca^{2+} currents (L and N) or tail Ca^{2+} currents (M and O, n = 10 for control, $Ca_V2.1$ α_1 OE and $Ca_V2.2$ α_1 OE). All data are shown as mean ± SEM. See also Table S1.
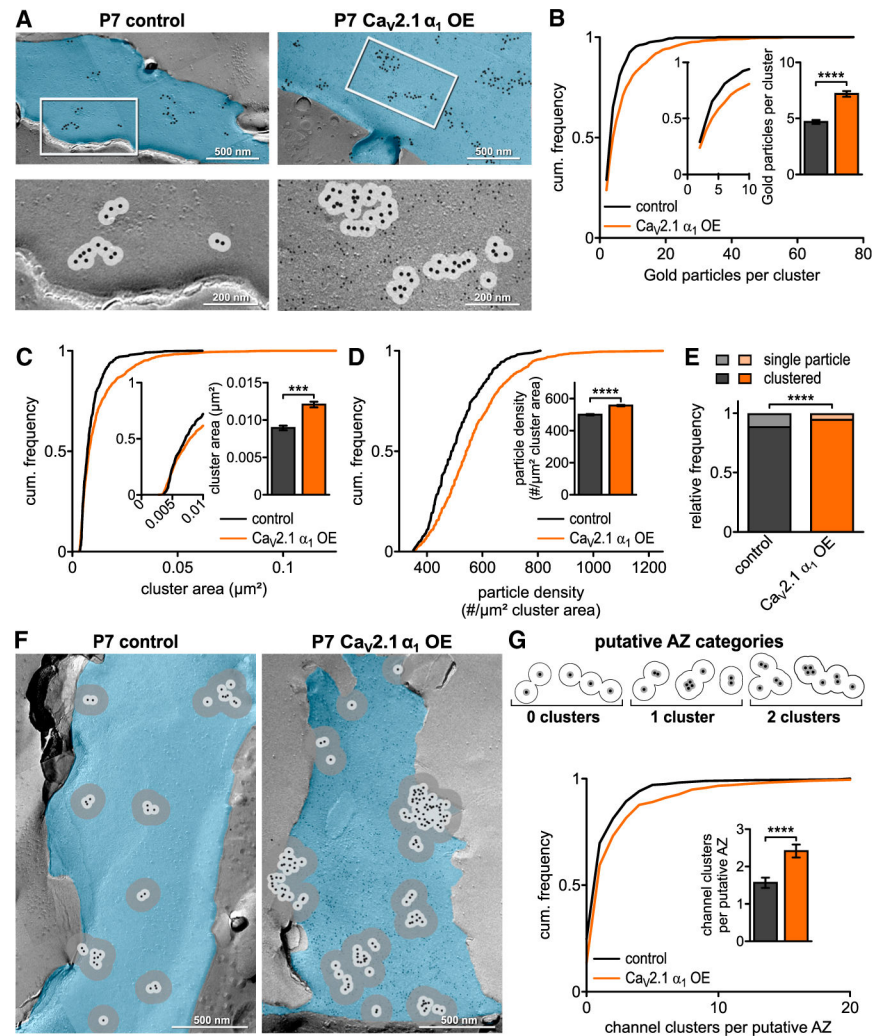
Figure 2. Ca$_V$2.1 α$_1$ OE Leads to Increase in Ca$_V$2.1 Channels and Clusters at Putative AZ at P7

(A) Representative SDS-digested freeze-fracture immunogold-labeled replicas of calyx P-faces (pseudocolored blue) of control and Ca$_V$2.1 α$_1$ OE at P7. (Top) Ca$_V$2.1 distribution. Large gold particles (12 nm) label Ca$_V$2.1, small gold particles (6 nm) label mEGFP (Ca$_V$2.1 α$_1$ OE only). (Bottom) High-magnification images of the boxed areas showing clustering of gold particles. A 30 nm circle indicates spatial uncertainty of Ca$_V$2.1 (light gray). Note that 12 nm gold particles have been enhanced for better visibility.

(B) Cumulative frequency distribution of gold particles per cluster; (insets) closeup of 0–10 particle clusters and corresponding bar graph ($p < 0.0001$, Mann-Whitney U test, n = 428 for control and n = 957 for Ca$_V$2.1 α$_1$ OE).

(C) Cumulative frequency distribution of cluster area; (inset) closeup of 0–0.01 μm^2 and corresponding bar graph ($p = 0.0006$, Mann-Whitney U test, n = 428 for control and n = 957 for Ca$_V$2.1 α$_1$ OE).

(D) Cumulative frequency distribution of gold particle density per μm^2 cluster area; (inset) bar graph ($p < 0.0001$, Mann-Whitney U test, n = 428 for control and n = 957 for Ca$_V$2.1 α$_1$ OE).

(E) Relative frequency of single channels to channel clusters at P7 ($p < 0.0001$, Fisher's exact test, n = 2,290 particles in 8 replicas for control and n = 7,314 particles in 7 replicas for $Ca_V2.1\ \alpha_1$ OE).

(F) Representative SDS-digested freeze-fracture immunogold-labeled replicas of calyx P-faces (blue) of control and $Ca_V2.1\ \alpha_1$ OE. Light gray circles indicate 30 nm radius, and dark gray circles indicate 100 nm radius around gold particles.

(G) (Top) Scheme of putative AZ categories. Cluster defined as overlap of at least two 30 nm circles and putative AZ as overlap of all 100 nm circles of clusters. (Bottom) Cumulative frequency distribution of channel cluster assembly within a putative AZ. (Inset) Number of clusters per putative AZ ($p < 0.0001$, Mann-Whitney U test, n = 271 for control and n = 390 for $Ca_V2.1\ \alpha_1$ OE). All data are shown as mean ± SEM. EM images are montage of multiple images assembled from the calyx P-face area containing $Ca_V2.1$. See also Table S2.
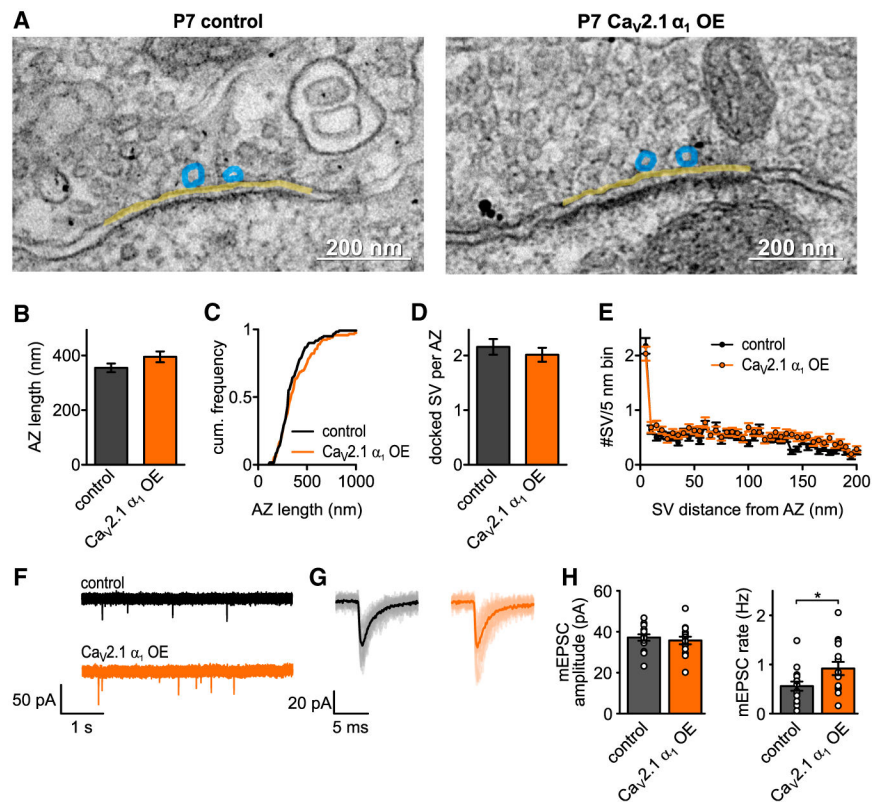
Figure 3. Ca_V2.1 α_1 OE Does Not Affect AZ Ultrastructure or Quantal Size at P7

(A–C) Representative EM images depicting AZs (yellow line) and docked SV (blue circles) of control (left) or Ca_V2.1 α_1 OE (right) calyces. Transduced terminals are identified by antibody-coupled gold nanoparticles directed against EGFP (black dots in right image). (B and C) AZ length (B, n.s., Mann-Whitney U test, n = 120 for control and n = 118 for Ca_V2.1 α_1 OE), cumulative frequency of AZ length (C).

(D) Number of docked vesicles per AZ (n.s., Mann-Whitney U test).

(E) SV distribution up to 200 nm distance from AZ in 5 nm bins.

(F) Representative traces of mEPSC recordings.

(G) Averaged mEPSCs for representative cell in (F).

(H) Average mEPSC amplitude (left, p = 0.56, two-tailed t test, n = 15) and mEPSC rate (right, p = 0.04, two-tailed t test). All data are shown as mean ± SEM. See also Table S2.
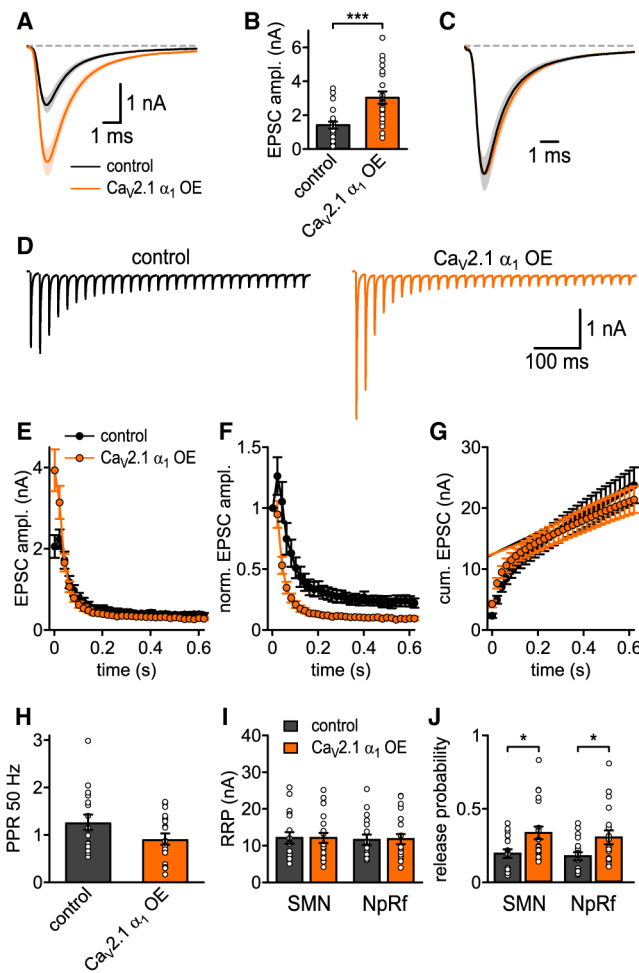
Figure 4. Increased Ca_V2.1 Levels at AZ Increase SV Release Probability at P7

(A) Average basal EPSC.

(B) EPSC peak amplitudes (p = 0.0006, Mann-Whitney U test, n = 20 for control and Ca_V2.1 α_1 OE).

(C) Basal EPSC normalized to peak.

(D) Average traces of 50 Hz EPSC trains for control (left, n = 17) and Ca_V2.1 α_1 OE (right, n = 20).

(E) 50 Hz train EPSC absolute peak amplitudes.

(F) 50 Hz train EPSC peak amplitudes normalized to first EPSC.

(G) Cumulative EPSC amplitudes.

(H) 50 Hz paired-pulse ratio (PPR, n.s., t test).

(I) RRP quantified with corrected SMN and NpRf methods (n.s., Mann-Whitney U test, n = 17 for control and n = 20 for Ca_V2.1 α_1 OE).

(J) Release probability P_r quantified with corrected SMN and NpRf methods (p = 0.033 and p = 0.045, respectively, Mann-Whitney U test). All data are shown as mean ± SEM. See also Table S3.
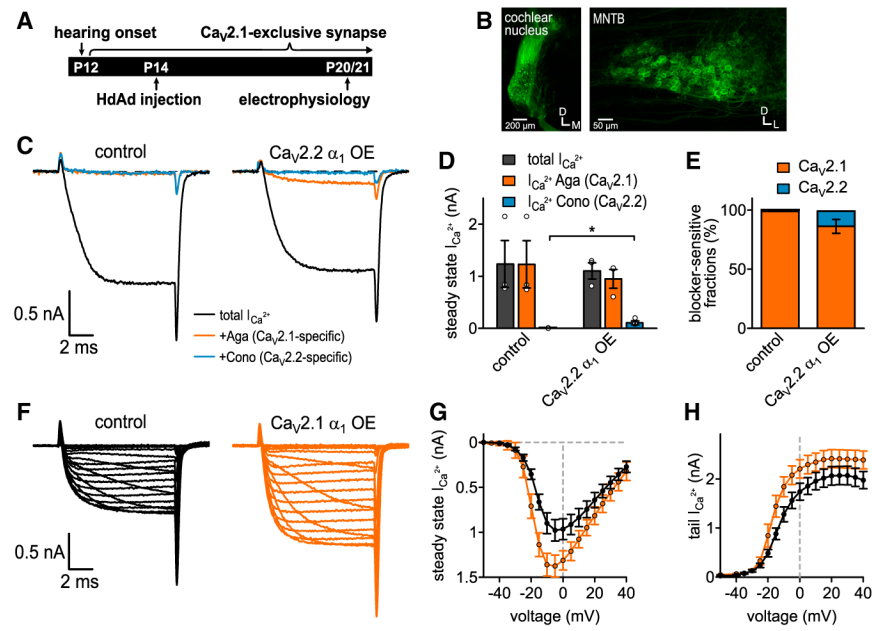
Figure 5. Ca$_V$2.2 α$_1$ OE Results in Slight Loss of Ca$_V$2.1 Currents, while Ca$_V$2.1 α$_1$ OE Results in an Increase in Ca$_V$2.1 Currents at P20/21 Calyx

(A) Experimental timeline from virus injection into CN at P14 to electrophysiological recordings at P20/21.

(B) Confocal images of brainstem slices injected with Ca$_V$2.1 α$_1$ OE construct. (Left) CN injection site. (Right) Contralateral MNTB with mEGFP-expressing calyx of Held terminals.

(C) Pharmacological isolation of Ca$_V$2 isoforms expressed in the presynaptic terminal at P21 in control (n = 3) and Ca$_V$2.2 α$_1$ OE (n = 3). Average current traces before application of blockers (black), after applying 200 nM ω-agatoxin IVA to specifically block Ca$_V$2.1 (Aga, brown) and after applying 2 μM ω-conotoxin GVIA to specifically block Ca$_V$2.2 (Cono, blue).

(D) Ca^{2+} current amplitudes before blocker application (black, n.s., two-tailed t test), Aga-sensitive Ca^{2+} current amplitudes (brown, n.s., one-tailed t test), and Cono-sensitive Ca^{2+} current amplitudes (blue, 0.016, one-tailed t test).

(E) Relative Ca^{2+} current fractions sensitive to blockers.

(F) Average Ca^{2+}-current traces to 10 ms step depolarizations from −80 mV holding to voltages between −50 and +40 mV for control (left, n = 9) and Ca$_V$2.1 α$_1$ OE (right, n = 10).

(G and H) Current-voltage relationships of either peak Ca^{2+} currents (G) or tail Ca^{2+} currents (H). All data are shown as mean ± SEM. See also Table S4.
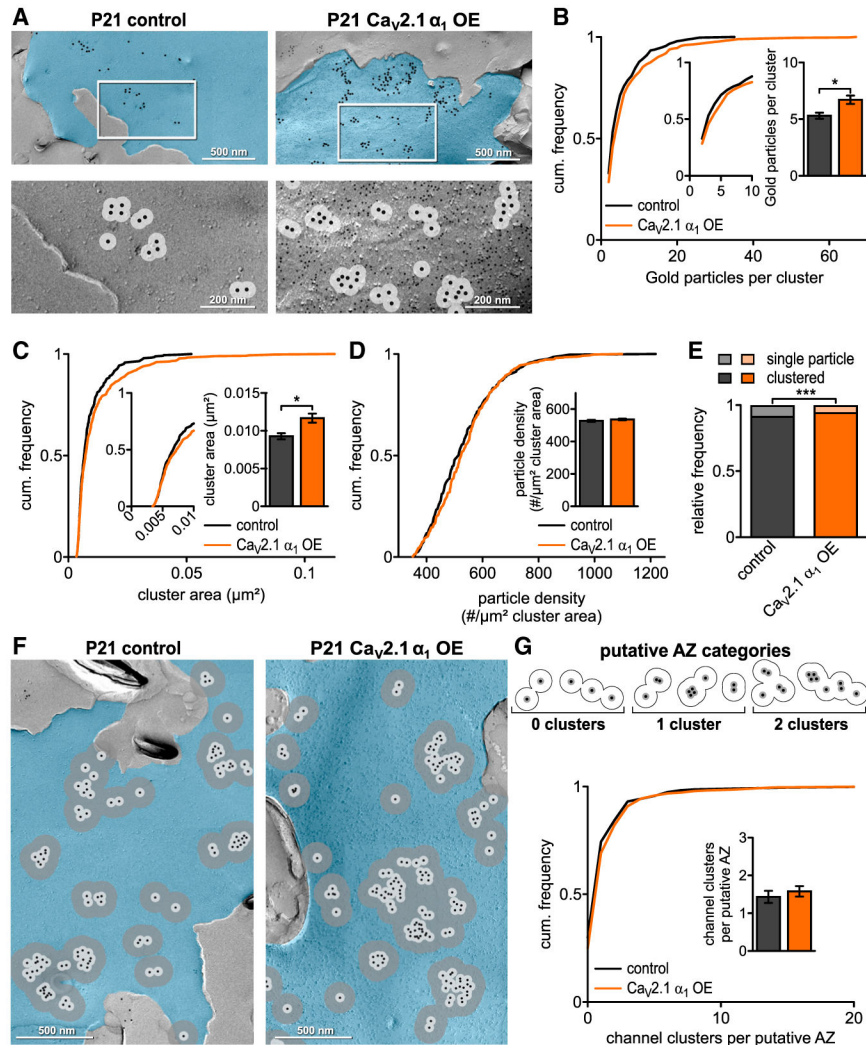

(E) Relative frequency of single channels to channel clusters (p = 0.0003, Fisher's exact test, n = 1,982 particles in 13 replicas for control and n = 3,307 particles in 10 replicas for $Ca_V2.1$ α_1 OE).

(F) Representative SDS-digested freeze-fracture immunogold labeled replicas of calyx P-faces (blue) of control and $Ca_V2.1$ α_1 OE at P21. Large gold particles (12 nm) label $Ca_V2.1$, small gold particles (6 nm) label mEGFP (control and $Ca_V2.1$ α_1 OE only), 30 nm circle (light gray), and 100 nm circle (dark gray).

(G) (Top) Diagram of putative AZ categories. Cluster defined as overlap of at least two 30 nm circles and putative AZ as overlap of all 100 nm circles of clusters. (Bottom) Cumulative frequency distribution of channel cluster assembly within a putative AZ. (Inset) Number of clusters per putative AZ (p = 0.0663, Mann-Whitney U test, n = 230 for control and n = 285 for $Ca_V2.1$ α_1 OE). All data are shown as mean ± SEM. EM images are a montage of multiple images assembled from the calyx P face area containing $Ca_V2.1$. See also Table S5.
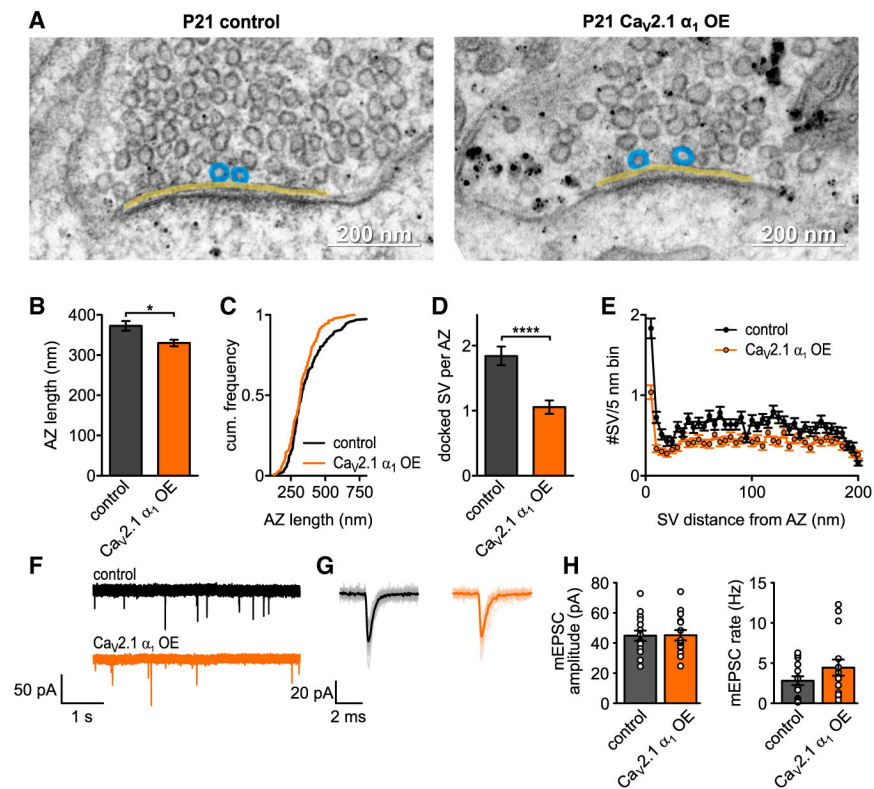
Figure 7. Ca$_V$2.1 α$_1$ OE Affects Presynaptic Ultrastructure without Affecting Quantal Size at P21

(A) Representative EM images depicting AZs (yellow line) and docked SV (blue circles) of control (left) or Ca$_V$2.1 α$_1$ OE (right) calyces. Transduced terminals identified by antibody-coupled gold nanoparticles directed against EGFP (black dots). (B and C) AZ length (B, p = 0.0339, Mann-Whitney U test, n = 160 for control and Ca$_V$2.1 α$_1$ OE), cumulative frequency of AZ length (C).

(D) Number of docked vesicles per AZ (p < 0.0001, Mann-Whitney U test).

(E) SV distribution up to 200 nm distance from AZ in 5 nm bins.

(F) Representative traces of mEPSC recordings.

(G) Averaged mEPSC recordings for representative cell in (F).

(H) Average mEPSC amplitude (left, p = 0.95, two-tailed t test, n = 15) and mEPSC rate (right, p = 0.35, Mann-Whitney U test). All data are shown as mean ± SEM. See also Table S5.
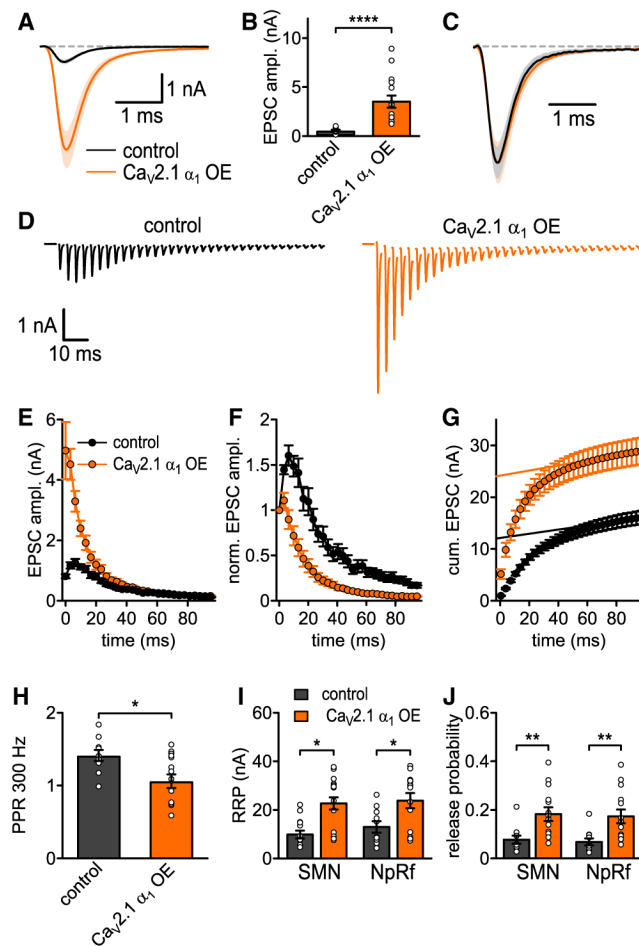
Figure 8. Increased Ca$_V$2.1 Levels at AZs Increase P_r and RRP Size at P20/21 Calyx

(A) Average basal EPSC.

(B) EPSC peak amplitudes (p < 0.0001, Mann-Whitney U test, n = 10 for control and n = 15 for Ca$_V$2.1 α_1 OE).

(C) Basal EPSC normalized to peak.

(D) Average 300 Hz EPSC trains for control (left, n = 10) and Ca$_V$2.1 α_1 OE (right, n = 14).

(E) 300 Hz train EPSC peak amplitudes.

(F) 300 Hz train EPSC absolute peak amplitudes normalized to first EPSC.

(G) Cumulative EPSC amplitudes.

(H) 300 Hz paired-pulse ratio (PPR, p = 0.04, t test).

(I) RRP quantified with corrected SMN and NpRf methods (p = 0.0109 and p = 0.0177, respectively, Mann-Whitney U test, n = 10 for control and n = 14 for Ca$_V$2.1 α_1 OE).

(J) Release probability P_r quantified with corrected SMN and NpRf methods (p = 0.0024 and p = 0.0067, respectively, Mann-Whitney U test). All data are shown as mean ± SEM. See also Table S6.

KEY RESOURCES TABLE

REAGENT or RESOURCE	SOURCE	IDENTIFIER
Antibodies		
Rabbit anti-GFP	Abcam	Cat# ab6556; RRID:AB_305564
Guinea pig anti-alpha 1A	Synaptic systems	Cat# 152205; RRID:AB_2619842
6 nm colloidal Gold-AffiniPure Donkey anti rabbit IgG	Jackson ImmunoResearch	Cat# 711005152; RRID:AB_2340585
12 nm colloidal Gold-AffiniPure Donkey anti guinea pig IgG	Jackson ImmunoResearch	Cat# 706205148; RRID:AB_2340465
Nanogold IgG goat anti rabbit IgG (H+L) Antibody	Nanoprobes	Cat# 2003; RRID:AB_2687591
Bacterial and Virus Strains		
HdAd 28E4 pun $Ca_V2.1$ α_1 syn mEGFP	Young Laboratory, University of Iowa	N/A
HdAd 28E4 pun $Ca_V2.1$ α_1 syn EGFP	Young Laboratory, University of Iowa	N/A
HdAd 28E4 pun $Ca_V2.2$ α_1 syn EGFP	Young Laboratory, University of Iowa	N/A
Chemicals, Peptides, and Recombinant Proteins		
Kynurenic acid	Tocris Bioscience	Cat# 0223
Lidocaine N-ethyl bromide (QX-314)	Sigma Aldrich	Cat# L5783
D-AP5	Tocris Bioscience	Cat# 0106
(−)-Bicuculline methochloride	Tocris Bioscience	Cat# 0131
Strychnine hydrochloride	Tocris Bioscience	Cat# 2785
4-Aminopyridine	Tocris Bioscience	Cat# 0940
Tetraethylammonium chloride	Sigma Aldrich	Cat# T-2265
Tetrodotoxin	Alomone labs	Cat# T-550
ω-Agatoxin AgaIVA	Alomone labs	Cat# STA-500
ω-Conotoxin GVIA	Alomone labs	Cat# C-300
Cadmium chloride hemi(pentahydrate)	Sigma Aldrich	Cat# C3141
Lucifer Yellow	Sigma Aldrich	Cat# L0259
Experimental Models: Organisms/Strains		
Mice: C57BL/6J	Jackson Laboratory	Cat# JAX:000664; RRID:IMSR_JAX:000664
Oligonucleotides		
Ad5 E1a (RCA) probe: NED-5'-AGCACCCCGGGC ACGGTTG-3'-MGBNFQ	This study	N/A
Ad5 E1a (RCA) fwd: 5'-GGGTGAGGAGTTTGTGT TAGATTATG-3'	This study	N/A
Ad5 E1a (RCA) rev: 5'-TCCTCCGGTGATAATGAC AAGA-3'	This study	N/A
E2B Iva2 (HV) probe: FAM-5'-TGTCTTTCAGTAGC AAGCT-3'-TAMRA	This study	N/A

REAGENT or RESOURCE	SOURCE	IDENTIFIER
E2B Iva2 (HV) fwd: 5'-TGGGCGTGGTGCCTAAAA-3'	This study	N/A
E2B Iva2 (HV) rev: 5'-GCCTGCCCCTGGCAAT-3'	This study	N/A
Genomic stuffer DNA (HdAd) probe: VIC-5'- AGC CTCTCTCATCTCACAGT -3'-MGBNFQ	This study	N/A
Genomic stuffer DNA (HdAd) fwd: 5'-CCCCGCTA CCCCAATCC-3'	This study	N/A
Genomic stuffer DNA (HdAd) rev: 5'-TTAGCTTTTT TGGGTGATTTTTCC-3'	This study	N/A
$Ca_V 2.1$ α_1 subunit cDNA (*Mus musculus*)	NCBI	NP_031604.3
$Ca_V 2.2$ α_1 subunit cDNA (*Mus musculus*)	NCBI	NP_001035993.1
Software and Algorithms		
Matlab	The Mathworks	RRID:SCR_001622; v9.3, v9.5
Patchmaster	HEKA; Harvard Bioscience	RRID:SCR_000034; v2×90.2
Igor Pro	Wavemetrics	RRID:SCR_000325; v6.37
Prism	Graphpad software	RRID:SCR_002798; v7.04
Fiji	https://fiji.sc/	RRID:SCR_002285
Fitmaster	HEKA; Harvard Bioscience	RRID:SCR_016233; v2×90.2
Patcher's Power Tools	Max Planck Institute for Biophysical Chemistry; Gottingen; Germany	RRID:SCR_001950; v2.19
Microscopy Image Browser	Electron Microscopy Unit; Institute of Biotechnology; University of Helsinki; Finland	RRID:SCR_016560; v2.4
StereoDrive	Neurostar	N/A; v3.1.5
Live Acquisition	Thermo Fisher Scientific	N/A; v2.1.0.10
QCapture	QImaging	RRID:SCR_014432; v7.0
NpRf model (Matlab function)	This study	https://doi.org/10.17632/4ycrjtpfc6.1